Phosphorylation of HP1/Swi6 relieves competition with Suv39/Clr4 on nucleosomes and enables H3K9 trimethyl spreading.

Dana R Kennedy[1,2], Joel Lemiere[3], Catherine Tan[3,4], Eric Simental[1,2], Julian Braxton[5,6], Robert A Maxwell[7], Ahmed AA Amine[1], and Bassem Al-Sady[1*].

[1]Department of Microbiology and Immunology and GW Hooper Foundation, UCSF, [2]TETRAD graduate program, UCSF [3]Biomedical Sciences graduate program, UCSF, [4]Department of Cell and Tissue Biology, UCSF, [5]Chemistry and Chemical Biology graduate program, UCSF, [6]Institute for Neurodegenerative Diseases, UCSF, [7]The Vincent J. Coates Proteomics/Mass Spectrometry Core Laboratory, University of California, Berkeley, CA, USA.

*bassem.al-sady@ucsf.edu

ABSTRACT

Heterochromatin formation in Schizosaccharomyces pombe requires the spreading of histone 3 (H3) Lysine 9 (K9) methylation (me) from nucleation centers by the H3K9 methylase, Suv39/Clr4, and the reader protein, HP1/Swi6. To accomplish this, Suv39/Clr4 and HP1/Swi6 have to associate with nucleosomes both nonspecifically, binding DNA and octamer surfaces and specifically, via recognition of methylated H3K9 by their respective chromodomains. However, how both proteins avoid competition for the same nucleosomes in this process is unclear. Here, we show that phosphorylation tunes the nucleosome affinity of HP1/Swi6 such that it preferentially partitions onto Suv39/Clr4's trimethyl product rather than its unmethylated substrates. Preferential partitioning enables efficient conversion from di-to trimethylation on nucleosomes in vitro and H3K9me3 spreading in vivo. Together, our data suggests that phosphorylation of HP1/Swi6 creates a regime that relieves competition with the "read-write" mechanism of Suv39/Clr4 for productive heterochromatin spreading.

INTRODUCTION

Heterochromatin is a gene-repressive nuclear structure conserved across eukaryotic genomes[1]. Heterochromatin assembly requires seeding at nucleation sites and lateral spreading over varying distances to define a silenced domain[2]. In one highly conserved heterochromatic system, the spreading process requires at least two components: First, a “writer” enzyme, a suppressor of variegation 3-9 methyltransferase homolog (Suv39, Clr4 in *S. pombe*), which deposits Histone 3 lysine 9 methylation (H3K9me)[3]. Spreading by this H3K9 methylation “writer” depends on a positive feedback relationship in which the “writer” also contains a specialized histone-methyl binding chromodomain (CD) that recognizes its own product, H3K9me[4,5]. Second, spreading then further requires a “reader” protein[3,6,7], Heterochromatin Protein 1 (HP1, Swi6 in *S. pombe*), that also recognizes H3K9me2/3 via a CD[8].

How do HP1 proteins execute their essential function in heterochromatin spreading? One manner in which they do so is by directly recruiting the Suv39 methyltransferase to propagate H3K9 methylation[9–11]. Second, HP1 proteins oligomerize on H3K9me-marked chromatin, which has been invoked as a mechanism that supports spreading[12]. HP1 oligomerization also underlies its ability to undergo Liquid-Liquid Phase Separation (LLPS) *in vitro* on its own or with chromatin[13–15], and condensate formation *in vivo*[13,14,16,17]. This condensate formation may promote spreading by providing a specialized nuclear environment that concentrates HP1 and its effectors[18] and/or excludes antagonists of heterochromatin[13]. The silencing of heterochromatin by HP1 may be coupled to spreading by oligomerization, which likely promotes chromatin compaction and blocks RNA polymerase access[19,20]. Silencing may also require oligomerization-independent mechanisms like HP1’s ability to bind RNA transcripts and recruit RNA turnover machinery[21,22].

However, these proposed mechanisms for HP1’s role in spreading do not contend with a central problem, which is that HP1 and Suv39/Clr4 directly compete for the same substrate on multiple levels. This competition can be specific, as HP1 and Suv39/Clr4 have CDs that recognize the H3K9me2/3 chromatin mark[12,23]. It is also non-specific, as both HP1 and Suv39/Clr4 bind DNA and histone octamer surfaces of the nucleosome substrate[5,17,23–26]. How can HP1 promote H3K9 methylation spreading by Suv39/Clr4 but not get in its way? One explanation for managing the specific competition is an observed difference in methylation state preference. Clr4, for example, is more selective for the terminal trimethylated (H3K9me3) state than Swi6 or the other HP1 paralog in *S. pombe,* Chp2[23]. However, how the significant H3K9me3- independent nucleosome affinity of Clr4 and Swi6 is coordinated to avoid competition is not clear.

65 One possible way to regulate competition in spreading is through post-translational
66 modifications of HP1. For example, HP1a, HP1α, and Swi6 are phosphorylated by CKII protein
67 kinases[27–29]. Phosphorylation of HP1 across species has been shown to regulate multiple of its
68 biochemical activities including LLPS[13], specificity for H3K9me[13,30], and affinity for nucleic
69 acids[30]. In *S. pombe*, several Swi6 *in vivo* phosphorylation sites have been documented in the
70 N-terminal extension (NTE), the CD, and the hinge domain[27], which, when mutated, disrupt
71 transcriptional gene silencing[27]. While HP1 phosphorylation has been known to be important for
72 its function for 20 years[31], the mechanisms by which phosphorylation-induced biochemical
73 changes in HP1 direct its cellular activity and coordination with H3K9 "writers" remain unclear.

74 In this study, we focused on previously identified Swi6 phosphorylation target sites[27] and found
75 that two sites in particular, S18 and S24, are required for the spreading, but not nucleation, of
76 heterochromatin. Spreading defects in Swi6 S18/24A mutants arise inability to convert
77 H3K9me2 to H3K9me3 outside creation sites. We show biochemically that the primary role of
78 phosphorylation is to lower Swi6's overall chromatin affinity. This lowered affinity preferentially
79 partitions Swi6 onto H3K9me3 nucleosomes, rather than unmethylated nucleosomes, *in vitro*
80 and into heterochromatin foci, rather than the nucleoplasm, *in vivo.* It may appear counter-
81 intuitive that lowered affinity should have this effect. However, since phosphorylation also
82 increases Swi6's propensity to oligomerize, this ultimately reduces the Swi6 pool available to
83 bind unmethylated sites. We propose that phosphorylation of Swi6 frees up Clr4's substrates for
84 efficient trimethylation, and thus, spreading.

85

86 **RESULTS**

87 *Serines 18 and 24 are necessary for heterochromatin spreading but not nucleation.*

88 Previously, several phosphoserines in Swi6 have been shown to play a role in heterochromatin
89 gene silencing[27] (**Figure 1A**). To address whether the phosphorylation targets play a role in
90 nucleation and/or spreading of heterochromatin, we used our mating type locus (MAT)
91 heterochromatin spreading sensor (HSS[32,33]) (**Figure 1B**). The HSS allows us to separate
92 nucleation and spreading events at single-cell resolution via three separate transcriptional
93 reporters: "green" at nucleation sites, "orange" at spreading sites, and "red" in a euchromatic
94 site to control cell-to-cell noise[32,33]. Specifically, we used a MAT locus HSS with only the *cenH*
95 nucleator intact (MAT *ΔREIII* HSS[33]), which enables us to isolate spreading from one nucleator.
96

97 To query *swi6* serine-to-alanine (S-A) mutants in this background, we first replaced the *swi6*
98 open reading frame with the *ura4* gene (*swi6::ura4*). Using homologous recombination, we then
99 replaced the *ura4* cassette with either wild-type or S-A mutant *swi6* open reading frames
100 followed by a kanamycin resistance marker (**Figure 1B**). We based our S-A mutations on the
101 phosphoserines previously identified in *Shimada et al.,* which include S18, S24, S46, and S52 in
102 the NTE, S117 in the CD, and S192, S212, and S220 in the hinge (**Figure 1A**). Here, we
103 constructed the following S-A mutants: S18A and S24A (*swi6*$^{S18/24A}$); S46A and S52A
104 (*swi6*$^{S46/52A}$); S46A, S52A, S117A, S192A, S212A, and S220A, (*swi6*$^{S46/52/117\text{-}220A}$, "S18/S24
105 available"); and S18A, S24A, S117A, S192A, S212A, and S220A (*swi6*$^{S18/24/117\text{-}220A}$, "S46/S52
106 available"). These mutants are expressed at similar levels compared to wild-type as assessed
107 by western blot, using a polyclonal anti-Swi6 antibody (**Figure 1C,** further validated by
108 cytometry in **SFigure 4C**). Note that not all phospho-site mutants yield an observable band shift
109 by SDS-PAGE gel, even though Swi6 in these mutants is expected to retain phosphorylation at
110 other sites. This was previously observed[27] and is likely because the sequence context of a
111 phosphorylated residue determines whether or not it will result in a bandshift[34].
112
113 When analyzed by flow cytometry, *Δswi6* cells exhibit a silencing defect in which both the
114 nucleation (green ON) and spreading (orange ON) reporters are expressed (**Figure 1D**).
115 Conversely, wild-type *swi6* cells show robust silencing of both reporters as we reported prior[33]
116 (orange 11.1% ON, **Figure 1E**). Mutating only S46 and S52 to alanines (*swi6*$^{S46/52A}$) largely
117 phenocopies wild-type *swi6* (orange 15% ON, **Figure 1F**). In contrast, mutation of serines at 18
118 and 24 (*swi6*$^{S18/24A}$) resulted in the loss of spreading (orange 92.4% ON), while largely
119 maintaining proper nucleation (green off) (**Figure 1G, SFigure 1A-C**). Restoring S18 and S24,
120 while mutating the other 6 serines to alanines (*swi6*$^{S46/52/117\text{-}220A}$) recovers much of the nucleation
121 and spreading observed in wild-type, though with a modest silencing loss at orange (orange
122 26.4% ON, **Figure 1H, SFigure 1D-F**). Thus, S18 and S24 play a dominant role in regulating
123 spreading, while other serines make a minor contribution. However, when only S46 and S52 are
124 available (*swi6*$^{S18/24/117\text{-}220A}$), cells not only exhibit a loss of spreading (orange 94.3% ON) but
125 also a moderate loss of silencing at the nucleator (green shifted towards ON) (**Figure 1I**). This
126 loss of silencing approaches but is not as severe as the deletion of *ckb1*, the gene encoding a
127 crucial regulatory subunit of the CKII kinase. This indicates that while the complete loss of Swi6
128 phosphorylation disrupts spreading (orange 82-83% ON versus 2.3% in the wild-type control,
129 **SFigure 1K, L**), it also affects silencing at the nucleator. However, this defect is not nearly as
130 severe as in *Δswi6* (**Figure 1D**), highlighting the role of Swi6 phosphorylation primarily in

131 spreading. Overall, we interpret these results to indicate that NTE S18-52 phosphorylation
132 contributes to regulating spreading, with S18/24 as major and 46/52 as minor
133 contributors. Phosphorylation of serines in the Swi6 CD and hinge make a further minor
134 contribution to Swi6's overall silencing role, which is revealed only in the context of S18/24A.
135 Given the greater loss of silencing revealed by *Δckb1,* we speculate that there are additional
136 CKII target residues in Swi6, a notion confirmed by our *in vitro* Mass Spectrometry (see below),
137 and that their phosphorylation contributes to Swi6's silencing role at the nucleator.
138

139 *Serines 18 and 24 are required for the spreading of H3K9me3 but not H3K9me2.*

140 We next asked how phosphorylation of S18 and S24 contributes to the propagation of
141 heterochromatic histone marks. We used chromatin immunoprecipitation followed by
142 sequencing (ChIP-seq) to address how levels of the heterochromatic marks, Histone 3 lysine 9
143 di- and trimethylation (H3K9me2/me3), are affected in the context of wild-type *swi6*, *swi6*$^{S18/24A}$,
144 and *Δswi6* in the MAT *ΔREIII* HSS background containing the "green" and "orange" reporters
145 (**Figure 2A**). Consistent with prior work, we define H3K9me2 as the heterochromatin structural
146 mark[35] and H3K9me3 as the heterochromatin spreading and silencing mark[7,35,36]. We first
147 examined the MAT locus. Note that we cannot make definite statements about ChIP-seq signals
148 over the "green" and "orange" reporters themselves, as the reporter cassettes harbor
149 sequences that are duplicated 3-4 times in the genome[32], making ChIP-seq read assignment
150 ambiguous. Overall, H3K9me2 levels at the MAT locus dropped significantly in *Δswi6,*
151 consistent with prior work[7]; however, *swi6*$^{S18/24A}$ mutant maintained similar levels of H3K9me2 to
152 wild-type *swi6* (**Figure 2B,** top). Examining the distribution more closely, at the *cenH* nucleator,
153 only *Δswi6* showed a minor decline of H3K9me2 in some regions. To the left of *cenH,* H3K9me2
154 levels decreased in *Δswi6* but not in *swi6*$^{S18/24A}$. To the right of *cenH,* H3K9me2 levels also
155 severely declined in *Δswi6,* while in *swi6*$^{S18/24A}$ they appear to drop moderately near *mat3M*, but
156 recovered to wild-type levels at IR-R. When examining H3K9me3, we observed a different
157 relationship: H3K9me3 patterns in *swi6*$^{S18/24A}$ much more closely mirrored *Δswi6*. Specifically, to
158 the left of *cenH,* H3K9me3 dropped to an intermediate level between wild-type and *Δswi6,* while
159 on the right of *cenH,* H3K9me3 levels closely matched *Δswi6 (***Figure 2B,** bottom). Importantly,
160 this behavior of H3K9me3 is consistent with our flow cytometry results (**Figure 1**), where
161 silencing is largely unaffected at "green" in *swi6*$^{S18/24A}$, while "orange" was expressed.
162

163 We wanted to further examine if the observation of H3K9me3 loss in *swi6*$^{S18/24A}$ versus wild-type
164 *swi6* held for other genome regions. When we analyzed the subtelomeric region (*tel IIR*) we
165 found that over the nucleation region *tlh2,* H3K9me2 levels are slightly elevated in *swi6*$^{S18/24A}$,
166 but then begin to drop ~6.4 kb to the left of *tlh2* (**Figure 2C,** top, red bar, and arrow).
167 Interestingly, H3K9me3 levels drop closer to the *tlh2* nucleator than H3K9me2*;* the 95%
168 confidence interval of wild-type and *swi6*$^{S18/24A}$ separate at the left edge of *tlh2* (**Figure 2C,**
169 bottom). This observation at the *tlh2* nucleator suggests the conversion of H3K9me2 to
170 H3K9me3 is inhibited right as heterochromatin structures exit nucleation centers. We observed
171 the same trend at the left subtelomere of chromosome I (*tel IL*, **SFigure 2B**). At the
172 subtelomere, spreading distances outside nucleation sites are longer than at other loci, thus this
173 loss of H3K9me3 just outside *tlh2* has the opportunity to manifest as an H3K9me2 spreading
174 defect several kilobases downstream. This result is consistent with the requirement of
175 Suv39/Clr4 methyltransferases to bind H3K9me3 for H3K9 methylation spreading[5,23]. We note
176 that the left telomere of chromosome II contains no annotated nucleators in the published
177 sequence. Hence, we could not observe the same trend there (*tel IIL,* **SFigure 2C**).
178 A similar defect in H3K9me3 spreading also occurs at the pericentromere (*cenII*), specifically,
179 from the outer repeat (*otr*) into the inner repeat (*imr*) (**Figure 2D**, bottom versus top). However,
180 the distances are likely too short from nucleation centers in *otr* to observe a resulting loss of
181 H3K9me2 (**Figure 2D**). We note no distinguishable differences in H3K9me2 and H3K9me3 at
182 *mei4*, a well-studied heterochromatin island (**SFigure 1A**).

183 Together, our ChIP-seq data show that *swi6*$^{S18/24A}$ is deficient in the conversion of H3K9me2 to
184 me3 outside nucleation centers, which results in loss of silencing and ultimately, the loss of
185 H3K9me2 spreading, as evident for the subtelomere.

186

187 *Swi6 phosphorylation increases oligomerization and decreases nucleosome affinity.*

188 Next, we wanted to pinpoint the biochemical mechanisms that can account for the spreading
189 defects in *swi6*$^{S18/24A}$ (**Figure 1G, Figure 2**). HP1 oligomerization has been linked to spreading[12].
190 In turn, HP1's intranuclear dynamics have been linked to how it engages chromatin[37–40]. We
191 thus probed if and how phosphorylation may impact these two properties of Swi6.

192 We used Size Exclusion Chromatography followed by Multi-Angle Light Scattering (SEC-MALS)
193 to probe oligomerization, and fluorescence polarization to quantify H3K9me3 peptide and
194 nucleosome binding. To produce phosphorylated Swi6 (pSwi6), we co-expressed Swi6 with

195 Caesin Kinase II (CKII) in *E. coli* (**Figure 3A**). We used 2-dimensional Electron Transfer
196 Dissociation Mass Spectrometry (2D ETD-MS) to identify which residues in pSwi6 are
197 phosphorylated and used unphosphorylated Swi6 (unpSwi6) as a control (**Figure 3B**). We found
198 that only pSwi6, and not unpSwi6, has detectable phosphorylated peptides. The residues
199 phosphorylated in pSwi6 include several that were identified *in vivo* (**Figure 1A,** S18, S24, S46,
200 S52, S117, S212, S220 but not S192) and some additional sites not previously identified (S43,
201 S45, S165, S224, S227). This detection of additional CKII target sites is likely because of the
202 higher sensitivity achieved in our 2D-ETD-MS experiments from purified protein: 1. 2D-ETD-MS
203 better preserves phosphorylation sites compared to other methods and is highly sensitive. 2
204 Pure, *in vitro*-produced protein of high yield is likely to result in more detection events than *in*
205 *vivo*-derived protein.

206 SEC-MALS traces of uncrosslinked pSwi6 and unpSwi6 reveal both proteins are estimated to
207 be of similar dimer mass, 90.8 kDa and 100.4 kDa respectively (**SFigure 3A**). However, pSwi6
208 elutes before Swi6, a trend similar to phosphorylated HP1α[13]. There is also a small shoulder in
209 the pSwi6 trace, indicating a minor fraction of higher-order oligomers (**SFigure 3A**, grey arrow).
210 As previously published[12], Swi6 crosslinking leads to the appearance of higher molecular weight
211 species. We observed that crosslinked Swi6 and pSwi6 elute as apparent dimers (93.4 and 86.2
212 kDa, respectively) and tetramers (210.6 and 180.8 kDa, respectively) (**Figure 3D**). However,
213 only pSwi6 additionally forms octamers (365.2kDa) and possibly even larger oligomers, as
214 indicated by a broad shoulder (**Figure 3D**).

215 We next quantified the binding of pSwi6 to H3K9me0 and H3K9me3 peptides by fluorescence
216 polarization (**Figure 3D**). pSwi6 binds to H3K9me0 and H3K9me3 peptides with affinities (K_d) of
217 227.4μM and 2.45μM, respectively, revealing a ~93X specificity for H3K9me3 (**Figure 3F**).
218 While we could not determine the H3K9me0 peptide K_d for unpSwi6, the K_d for the H3K9me3
219 peptide was 8.17 μM (**Figure 3D**, **F**). Previously, the specificity for unpSwi6 was reported at
220 ~130X[12], thus indicating little difference in H3K9me3 peptide specificity between the two
221 proteins. We note that consistent with previous reports on total cellular Swi6[35], recombinant
222 pSwi6 also shows a ~2.2X preference for H3K9me3 versus H3K9me2 peptides (**SFigure 3E**).

223 We next probed how phosphorylation affects nucleosome binding. We performed fluorescence
224 polarization with fluorescently labeled nucleosomes that are unmethylated (H3K9me0) or
225 trimethylated ($H3K_c9me3$)[41,12]. Phosphorylation had no impact on the specificity for the
226 H3K9me3 mark, consistent with the peptide observation (19.4X, vs. 19X for unpSwi6 or pSw6,
227 respectively, **Figure 3E**, **F**).

228 However, we observe a 12X difference in affinity to the nucleosome overall between pSwi6 and
229 Swi6 (**Figure 3F**). The H3K$_c$9me3 nucleosome affinity is 0.12 μM and 1.45 μM for unpSwi6 and
230 pSwi6, respectively, while the H3K9me0 affinity is 2.33 and 27.5 μM, respectively. We note the
231 affinity of pSwi6 to the H3K$_c$9me3 nucleosome is similar to its affinity to the H3K9me3 peptide,
232 binding only 1.7X tighter to the H3K$_c$9me3 nucleosome (1.45μM vs. 2.45μM). Instead, and
233 consistent with previous results, unpSwi6 binds 68X more tightly to the nucleosome than to the
234 tail (8.17 μM for the H3K9me3 tail versus 0.12μM for H3Kc9me3), which is thought to arise from
235 additional contacts beyond the H3 tail on the nucleosome.

236 Why would a 12X lower affinity towards the nucleosome substrate be advantageous for pSwi6's
237 function in spreading (**Figure 1**,**2**)? In the literature, the cellular abundance of Swi6 is measured
238 at 9000- 19,400 molecules per cell[42,43]. The estimated fission yeast nuclear volume of ~7mm^3
239 [44,45] then yields an approximate intranuclear Swi6 concentration of ~2.1 -4.6μM. Given our
240 measured nucleosome K$_d$s (**Figure 3F**), the intranuclear concentration of unpSwi6 would
241 theoretically be above its K$_d$ for both H3K9me0 and me3 nucleosomes. The concentration of
242 pSwi6 would exceed its K$_d$ for H3K$_c$9me3 but be significantly below (~10X) its K$_d$ for H3K9me0
243 nucleosomes. We cannot assume the same fraction of bound nucleosome from *in vitro*
244 measurements applies *in vivo*, because nucleosome concentrations in the cell (~10μM based
245 on accessible genome size and average nucleosome density[46,47]) greatly exceed what is used
246 in a binding isotherm. We can use a quadratic equation[48] (see methods) appropriate for these *in*
247 *vivo* regimes instead of a typical K$_d$ fit to estimate the fraction bound. As only 2% of the *S.*
248 *pombe* genome is heterochromatic, we approximate the total nucleosome concentration (10μM)
249 to reflect unmethylated nucleosomes. The small, methylated nucleosome pool will mostly be
250 bound by Swi6 irrespective of the phosphorylation state. However, we estimate that only 5% of
251 unmethylated nucleosomes would be bound by pSwi6, while this would be ~16% for unpSwi6.
252 At the high end of the Swi6 concentration estimate, this fraction bound would increase to 30% of
253 unmethylated nucleosomes. Further, we expect enhanced oligomerization of pSwi6 on
254 heterochromatin to reduce the free Swi6 pool (see discussion). Therefore, we predict that the
255 main function of phosphorylation is to limit the partitioning of Swi6 into the unmethylated pool,
256 confining it to heterochromatin.

257 One test of this prediction would be altered localization of wild-type and phosphorylation
258 defective Swi6 versions in the fission yeast nucleus. Across species, HP1 homologs have been
259 shown to localize into heterochromatic foci *in vivo* and form LLPS droplets *in vitro* [13,14,16,37].
260 Specifically, phosphorylation of the NTE in human HP1α is one driver of heterochromatin foci

261 formation[13,38]. We investigated whether the loss of phosphorylation sites that impair
262 heterochromatin spreading (**Figure 1**, **2**) impacted partitioning between heterochromatin foci
263 and regions outside these foci, likely representing H3K9 unmethylated nucleosomes. We C-
264 terminally tagged wild-type *swi6* and phospho-serine mutants at the native locus with super fold-
265 GFP (Swi6-GFP), as an N-terminal tag disrupt Swi6 dimerization and oligomerization[25]. We
266 crossed these strains into a background containing *sad1*:mKO2, a spindle pole body (SPB)
267 marker (**SFigure 4A**). We chose this background, as Sad1 denotes the position of
268 pericentromeric heterochromatin[49,50] and can help orient other heterochromatin sites relative to
269 it. We examined the following SF-GFP tagged mutant variants: *swi6*$^{S18/24A}$, *swi6*$^{S46/52A}$,
270 *swi6*$^{S46/52/117-220A}$ (S18/S24 available), *swi6*$^{S18/24/117-220A}$ (S46/S52 available) (**Figure 1G-I**) and
271 imaged these strains by confocal microscopy (**Figure 3G**, **SFigure 4B**). Largely, these
272 mutations do not impact either Swi6 accumulation (**SFigure 4C**), nuclear foci number (**SFigure**
273 **4D**), or position of the foci relative to the SPB[51] (**SFigure 4E**, **F**).

274 We next quantified the accumulation of Swi6-GFP in foci. Unlike foci number or spatial
275 arrangement, the average foci intensity for Swi6-GFP strains carrying the S18/24A mutations is
276 significantly decreased relative to wild-type Swi6-GFP (**Figure 3H**), while the nucleoplasmic
277 signal increases. Because total Swi6-GFP levels do not change in these mutants (**SFigure 4C**),
278 this result indicates that Swi6$^{S18/24A}$-GFP and Swi6$^{S18/24/117-220A}$ -GFP molecules partition away
279 from heterochromatin foci. This finding is consistent with our prediction based on our *in vitro*
280 measurements and implies that Swi6 molecules that cannot normally be phosphorylated
281 partition onto unmethylated nucleosomes.

282

283 *Swi6 phosphorylation facilitates the conversion of H3K9me2 to me3 by Clr4.*

284 As unmethylated nucleosomes are Clr4's substrates, another prediction emerges. Since
285 unpSwi6 is more likely to bind unmethylated nucleosomes, Swi6 phosphorylation mutants may
286 interfere with Clr4 substrates, which could explain the defect in H3K9me2 to me3 conversion in
287 *swi6*$^{S18/24A}$ (**Figure 2**), the slowest transition catalyzed by Clr4[23]. For Swi6 phosphorylation to
288 prevent the conversion of H3K9me to me3, the Swi6 cellular pool would have to be mostly in the
289 phosphorylated state. To test this, we asked what fraction of Swi6 molecules in the cell are
290 phosphorylated at S18 and S24. We addressed this question by a quantitative western blot
291 approach, using two antibodies: a polyclonal Swi6 antibody[25] to detect all Swi6 molecules and a
292 phospho-serine antibody specific to phosphorylation at S18 and S24 (top blot vs. bottom blot,

293 respectively, **Figure 4A**). A standard curve of recombinant pSwi6 allowed us to quantify the total
294 pool of Swi6 molecules vs. those phosphorylated at S18 and S24. The *swi6*$^{S18/24A}$ mutant control
295 shows these phospho-serine antibodies are indeed specific (**Figure 4A**). We showed that the
296 majority of cellular Swi6 is phosphorylated at S18 and S24 (**Figure 4A** and **SFigure 5A**), 70%
297 and 100% across two biological replicate experiments.

298 We next tested if Swi6 phosphorylation directly impacted the ability of Clr4 to produce
299 H3K9me3. We incubated pSwi6 or unpSwi6 with Clr4 and monitored the conversion of the
300 H3K9me2 substrate to H3K9me3 under single turnover conditions[23] (**Figure 4B**). pSwi6 shows
301 an *in vitro* preference for H3K9me3 versus H3K9me2 peptides (**SFigure 3E**), suggesting that
302 phosphorylation may partition Swi6 towards H3K9me3 versus me0, but also, to some extent,
303 towards H3K9me3 versus me2.

304 We observed that the presence of unpSwi6 inhibits the conversion of H3K9me2 to H3K9me3 in
305 a concentration-dependent manner, but that this inhibition is significantly alleviated by pSwi6
306 (**Figure 4C** and **SFigure 5B,C**). Note we observe inhibition at the lowest concentration, 5μM,
307 which is near the estimated *in vivo* concentration of Swi6. When normalizing to H4 and fitting
308 H3K9me3 to k_{obs}, Clr4 methylation rates are significantly slowed in the presence of unpSwi6,
309 while pSwi6 reduces this inhibition (**Figure 4D**, **E**).

310 While these data could explain the H3K9me3-spreading defect, we observe for *swi6*$^{S18/24A}$
311 (**Figure 2**), our *in vitro*-produced pSwi6 is phosphorylated at multiple residues. Given that S18
312 and S24 only represent around 1/6 of the detected phosphorylation sites (**Figure 3B**), we
313 cannot necessarily conclude whether the biochemical phenotypes we observe depend on S18
314 and S24 phosphorylation. To examine this, we expressed and purified a phospho-mutant
315 protein, pSwi6$^{S18/24A}$, in which S18 and S24 are mutated to alanines and co-expressed it with
316 CKII. pSwi6$^{S18/24A}$ is still phosphorylated to a similar degree as pSwi6, which is apparent by the
317 similar gel migration shift observed for both proteins (**SFigure 3B**,**C**). Upon phosphatase
318 treatment, pSwi6$^{S18/24A}$ and pSwi6 adopt the same migration pattern as unpSwi6 (**SFigure 3B**,
319 **C**). 2D ETD-MS analysis of pSwi6$^{S18/24A}$ additionally confirmed a similar phosphopeptide pattern
320 to pSwi6, though with small changes in phosphopeptide prevalence (**SFigure 3D**).

321 We examined nucleosome affinity of pSwi6$^{S18/24A}$ compared to pSwi6 via fluorescence
322 polarization and found that pSwi6$^{S18/24A}$ shows increased affinity towards both the H3K9me0 and
323 K_c9me3 nucleosomes, 4.5 and 2.6X, respectively (**Figure 4F**). This result is consistent with S18
324 and S24 phosphorylation sites acting to modulate Swi6's chromatin affinity. However, since the

325 change in affinity for pSwi6$^{S18/24A}$ is less than the 12X loss observed for unpSwi6 vs. pSwi6, this
326 implies that other phosphoserines also contribute to lowering nucleosome affinity.

327 Overall, this data suggests a model whereby Swi6 NTE phosphorylation, particularly at S18 and
328 S24, partitions Swi6 away from binding the unmethylated substrate of Clr4 *in vivo,* which is likely
329 enhanced by increased Swi6 oligomerization at heterochromatin sites. Together, both reduced
330 affinity and oligomerization mechanisms promote the H3K9me3 spreading reaction.

331
332 **DISCUSSION**
333
334 Previous work[27] identified key Swi6 phosphoserines that regulate transcriptional gene silencing.
335 In this work, we find that Swi6 phosphoserines 18 and 24 are required for heterochromatin
336 spreading, but not nucleation (**Figure 1**). Swi6 phosphorylation promotes oligomerization, and
337 tunes Swi6's overall chromatin affinity to a regime that allows Clr4 to access its substrate
338 (**Figure 3**), facilitating the conversion of dimethyl H3K9 to the repressive and spreading-
339 promoting trimethyl H3K9 state (**Figure 4**). This modulation of chromatin affinity *in vivo* restricts
340 Swi6 to heterochromatin foci (**Figure 3, Figure S4**), which suggests that phosphorylation of
341 HP1 molecules may be required for their concentration into the heterochromatic compartment.
342 Three central themes emerge from this work:

343 *Swi6 phosphorylation decreases chromatin affinity, but not specificity.*
344 Phosphorylation is known to regulate HP1's affinity with itself[13], DNA[30,38], and chromatin[30,38], but
345 in manners that are homolog-specific. For example, phosphorylation in the NTE of HP1α
346 induces LLPS, but not for HP1a in *Drosophila*, where phosphorylation instead regulates
347 chromatin binding[16,31,52]. Underlying this may be that CKII target sequences are not conserved
348 across HP1s, for example, HP1α is phosphorylated in a cluster of 4 serines at the NTE (S11-
349 14)[29], HP1a only at S15 in the NTE, and S202 C-terminal to the CSD[31], whereas we report here
350 Swi6 is phosphorylated by CKII in the NTE, CD, and hinge (**Figure 3B**).
351
352 Phosphorylation increases the affinity towards H3K9me3 and H3K9me0 peptides both for Swi6
353 (**Figure 3D**) and HP1α[38]. However, the impact on nucleosome specificity is different across
354 species. Our data here shows that phosphorylation of Swi6 does not affect its specificity for both
355 H3K9me0 and H3Kc9me3 nucleosomes (**Figure 3E**, **F**), but phosphorylation of HP1α and HP1a
356 was reported to increase its specificity for H3K9me3 nucleosomes[13,30]. Instead, Swi6
357 phosphorylation decreases overall nucleosome affinity for unmethylated and H3Kc9me3
358 nucleosomes to a similar degree, 11.8X and 12X respectively, in contrast to HP1α[30,53]. What

359 may explain these differences? Internal interactions between the NTE, CD, hinge, and CSD
360 work together to drive nucleosome binding[17,25]. We speculate that these domain interactions are
361 differentially impacted by 1. the unique phosphorylation patterns in different HP1 orthologs (see
362 above) and 2. divergence in Swi6 amino acid sequence and size of the NTE and hinge that
363 harbor most CKII target sites. Both these differences result in unique outcomes with respect to
364 nucleosome specificity and affinity in different HP1 orthologs. Cross-linking mass spectrometry
365 studies indicate that the NTE of HP1α[54], as well as Swi6[17], contact the C-terminus of
366 H2A.Z/H2A, respectively, H2B, and the core (HP1α) and tail (Swi6) of H3, among other
367 contacts. NTE phosphorylation may specifically decrease these contacts, leading to detachment
368 from the nucleosome core.
369
370 This overall decrease in affinity partitions pSwi6 in a different way than unpSwi6, restricting
371 access of pSwi6 to chromatin inside nuclear foci. This is supported by our imaging data (**Figure**
372 **3**, **SFigure 4**) but is also consistent with data from human HP1α[38] and *in vivo* diffusion
373 measurements in the *swi6 sm-1* mutant. This mutant likely disrupts NTE phosphorylation and
374 shows greater residence outside heterochromatin[39]. Further, it is likely that increased
375 oligomerization of pSwi6 additionally strengthens this partitioning onto heterochromatin (next
376 section). A separate consequence of this affinity decrease is the relief of competition with Clr4
377 for the nucleosome substrate (**Figure 4**, see third section below).

378 *Swi6 phosphorylation increases oligomerization.*

379 Swi6 has been shown to form dimers and higher-order oligomers. Swi6 oligomerization across
380 chromatin has been linked to heterochromatin spreading *in vivo*[12]. Here, we show that
381 phosphorylation increases the fraction of oligomeric states, revealing octamers and possibly
382 higher molecular weight species (**Figure 3**). Swi6 exists in a closed dimer that inhibits the
383 spreading competent state, or an open dimer that promotes oligomerization[25]. One way pSwi6
384 could form higher molecular weight oligomers is by phosphorylation shifting the equilibrium from
385 the closed dimer to the open dimer[25]. We speculate the following thermodynamic consequence
386 of phosphorylation on the nuclear Swi6 pool: Oligomerization will be driven at sites of high Swi6
387 accumulation, which is likely near its high-affinity H3K9me3 nucleosome target. If this is true,
388 oligomerization will reduce the pool of free Swi6 available to engage unmethylated nucleosomes
389 even further, and below the theoretical level we described above (~5%).

390 HP1 proteins, like Swi6, form foci *in vivo,* which are associated with condensate formation,
391 rooted in HP1 oligomerization[13,16,17]. The reduction of GFP-Swi6$^{S18/24A}$ in nuclear foci we

392 observe (**Figure 3**) may be due to defects in condensate formation, or simply that fewer Swi6
393 molecules are available to form heterochromatic condensates. As discussed above, we expect
394 defects in phosphorylation to steer Swi6 toward unmethylated chromatin sites. The reduction of
395 GFP signal in Swi6$^{S18/24A}$ mutant foci may thus be due to losing Swi6 molecules to the
396 nucleoplasmic space.

397 *Phosphorylation of Swi6 enables H3K9 trimethylation by Clr4.*

398 Achieving H3K9 trimethylation is essential for both gene silencing and heterochromatin
399 spreading by Suv39/Clr4 enzymes[5,23]. For heterochromatin spreading, this is due to the positive
400 feedback loop within Suv39/Clr4, which depends on binding trimethyl H3K9 tails via the
401 CD[23,35,55].

402 For Clr4, the conversion from H3K9me0 to me1 and H3K9me1 to me2 is 10X faster than the
403 conversion from H3K9me2 to me3[23]. This slow step requires significant residence time on the
404 nucleosome and is thus highly sensitive to factors promoting or antagonizing Clr4 substrate
405 access, as well as nucleosome density[56]. Clr4 and Swi6 both make extensive contacts with
406 nucleosomal DNA and the octamer core[17,24]. unpSwi6 and Clr4 affinity to H3K9me0
407 nucleosomes are very similar (1.8μM and 2.3μM for Clr4[23] and Swi6, respectively), but nuclear
408 Swi6 concentration (2-4 μM) is likely higher than the Clr4 concentration[57]. Thus, unpSwi6 would
409 compete and displace Clr4 from its substrate. However, pSwi6's affinity for the H3K9me0
410 nucleosome (28μM) is in a regime that is well above its predicted *in vivo* concentration. Any
411 residual competition between pSwi6 and Clr4 would be mitigated by this lower affinity and the
412 likely higher affinity of the Clr4 complex to its *in vivo* nucleosome substrate, driven by additional
413 chromatin modfications[58].

414 This lowered pSwi6 nucleosome affinity likely relieves the trimethylation inhibition we observe
415 for unpSwi6 (**Figure 4**). Therefore, we propose that a major outcome of Swi6 phosphorylation is
416 to clear nucleosome surfaces for Clr4 to access its substrate (**Figure 4G**). An alternative, and
417 non-exclusive, possibility is that the reduced affinity of pSwi6 to trimethyl nucleosomes may also
418 limit the ability of Clr4/Suv39 to spread across nucleosomes, which requires the engagement of
419 its CD[23]. While the K_c9me3 nucleosome K_d of pSwi6 is just below its predicted *in vivo*
420 concentration, the fraction bound at trimethylated nucleosomes *in vivo* would be expected to
421 somewhat lower than for unpSwi6. We note, that instead of starting with H3K9me0
422 nucleosomes, we examined the conversion of H3K9me2 to me3. pSwi6 may have increased
423 affinity to those H3K9me2 than H3K9me0 substrates[43]. However, it has been shown by us
424 (**SFigure 3E**) and others[35] that pSwi6 or Swi6 isolated from *S. pombe* cells, which is mostly

425 phosphorylated (**Figure 4A**), has a preference for H3K9me3 over H3K9me2[35]. This lower
426 H3K9me2 preference may still help pSwi6 distinguish between binding H3K9me2 versus me3
427 chromatin *in vivo*, and not just H3K9me0 versus H3K9me3.

428 Our *in vivo* data (**Figures 1- 3**) reveals several serines in Swi6 contribute to spreading, but S18
429 and S24 have a dominant effect. The contribution of other serines is highlighted by 1. A change
430 in nucleosome affinity in pSwi6$^{S18/24A}$ that is 3-4X less than for unpSwi6 (**Figure 4F and Table**
431 **1**), and, 2. The additional phenotype of *swi6*$^{S18-220A}$ in gene silencing compared to *swi6*$^{S18/24A}$
432 (**Figure 1**, **SFigure 1**). Still, why might these two residues, when mutated, have a strong impact
433 on heterochromatin spreading? It is possible that phosphorylation of S18 and S24 plays a
434 disproportional role versus other residues in shifting the Swi6 from the closed to the open state.
435 Alternatively, it is possible that *in vivo*, phosphorylation at S18 and S24 are involved in the
436 recruitment of H3K9me3-promoting factors, including Clr3, and also other factors like
437 Abo1[36,59,60]. Prior work [27] has shown that Clr3 recruitment to heterochromatin is somewhat
438 compromised in *swi6*$^{S18-117A}$, while the recruitment of the anti-silencing protein Epe1 is
439 increased. While this loss of Clr3 and gain of Epe1 may be an indirect consequence of
440 compromised heterochromatin in *swi6*$^{S18-117A}$, it cannot be excluded that phosphorylation at S18
441 and S24 is necessary to help recruit Clr3 and/or exclude Epe1. This would provide another
442 mechanism for Swi6 to support trimethylation spreading by Clr4. Whether this is the case
443 requires further investigation.

444 Together, we believe that our work resolves a critical problem in heterochromatin biology, which
445 is how “writers” and “readers” promote heterochromatin spreading if they compete for the same
446 substrate surfaces. Phosphorylation of Swi6 tunes the partitioning of Swi6 between
447 unmethylated and methylated nucleosomes *in vivo,* such that Clr4 unmethylated substrates
448 remain largely unbound. Whether this phosphorylation is regulated temporally, at different
449 stages of heterochromatin formation, or spatially, at nucleation versus spreading sites, remains
450 to be investigated.

451

452 **LIMITATIONS OF THIS STUDY**

453 In this study, we examine how the phosphorylation of Swi6, especially at S18 and S24, impacts
454 its association with chromatin and interaction with Clr4/Suv39 and, ultimately, heterochromatin
455 spreading. We connect the loss of H3K9 trimethyl spreading and delocalization from
456 heterochromatin foci in *swi6*$^{S28/24A}$ mutants *in vivo* to an increased affinity for unmethylated

457 nucleosomes by unpSwi6. However, it is possible that phosphorylation at S18 and S24 is
458 important for the specific recruitment of Swi6 into heterochromatin foci by other factors. Our
459 study does not directly address this possibility. Our biochemical work does not provide direct
460 insight into why S18 and S24 are dominant *in vivo* compared to other phospho-serines. Further,
461 while we show that pSwi6 drives increased oligomerization, we have no direct evidence that
462 increased oligomerization via phosphorylation *in vivo* supports H3K9 trimethyl spreading. This
463 would require uncoupling phosphorylation from oligomerization, which we have not been able to
464 do so far. Our kinetic studies focus on the impact of Swi6 phosphorylation on the conversation
465 of H3K9me2 to me3. While Swi6 does prefer H3K9me3 over me2, we do not know if this
466 preference is sufficient *in vivo* to decrease the residence of pSwi6 on H3K9me2 enough not to
467 inhibit Clr4/Suv39 and support conversion to H3K9me3. Finally, while we show inhibition of this
468 conversion by unpSwi6, our study does not address whether unpSwi6 and Clr4/Suv39 occupy
469 the exact same surfaces on the nucleosome. Theoretically they could co-occupy the
470 nucleosome, and antagonism by unpSwi6 may utilize a mechanism other than
471 displacement/occlusion.

472

473 **REFERENCES**
474

475 1. Grewal, S. I. S. The molecular basis of heterochromatin assembly and epigenetic inheritance.
476 *Mol. Cell* **83**, 1767–1785 (2023).
477 2. Hamali, B., Amine, A. A. A. & Al-Sady, B. Regulation of the heterochromatin spreading
478 reaction by trans-acting factors. *Open Biol.* **13**, 230271 (2023).
479 3. Elgin, S. C. & Reuter, G. Position-effect variegation, heterochromatin formation, and gene
480 silencing in Drosophila. *Cold Spring Harb Perspect Biol* **5**, a017780 (2013).
481 4. Zhang, K., Mosch, K., Fischle, W. & Grewal, S. I. S. Roles of the Clr4 methyltransferase
482 complex in nucleation, spreading and maintenance of heterochromatin. *Nat Struct Mol Biol*
483 **15**, 381–8 (2008).
484 5. Muller, M. M., Fierz, B., Bittova, L., Liszczak, G. & Muir, T. W. A two-state activation
485 mechanism controls the histone methyltransferase Suv39h1. *Nat Chem Biol* **12**, 188–93
486 (2016).
487 6. Noma, K. *et al.* RITS acts in cis to promote RNA interference-mediated transcriptional and
488 post-transcriptional silencing. *Nat Genet* **36**, 1174–80 (2004).
489 7. Hall, I. M. *et al.* Establishment and maintenance of a heterochromatin domain. *Science* **297**,
490 2232–2237 (2002).
491 8. Jacobs, S. A. & Khorasanizadeh, S. Structure of HP1 chromodomain bound to a lysine 9-
492 methylated histone H3 tail. *Science* **295**, 2080–3 (2002).
493 9. Haldar, S., Saini, A., Nanda, J. S., Saini, S. & Singh, J. Role of Swi6/HP1 self-association-
494 mediated recruitment of Clr4/Suv39 in establishment and maintenance of heterochromatin in
495 fission yeast. *J Biol Chem* **286**, 9308–20 (2011).
496 10. Jenuwein, T. & Allis, C. D. Translating the histone code. *Science* **293**, 1074–80 (2001).

497 11. Aagaard, L., Schmid, M., Warburton, P. & Jenuwein, T. Mitotic phosphorylation of
498 SUV39H1, a novel component of active centromeres, coincides with transient accumulation at
499 mammalian centromeres. *J. Cell Sci.* **113 (Pt 5)**, 817–829 (2000).
500 12. Canzio, D. *et al.* Chromodomain-mediated oligomerization of HP1 suggests a
501 nucleosome-bridging mechanism for heterochromatin assembly. *Mol. Cell* **41**, 67–81 (2011).
502 13. Larson, A. G. *et al.* Liquid droplet formation by HP1α suggests a role for phase
503 separation in heterochromatin. *Nature* **547**, 236–240 (2017).
504 14. Sanulli, S. & J Narlikar, G. Liquid-like interactions in heterochromatin: Implications for
505 mechanism and regulation. *Curr. Opin. Cell Biol.* **64**, 90–96 (2020).
506 15. Keenen, M. M. *et al.* HP1 proteins compact DNA into mechanically and positionally
507 stable phase separated domains. *eLife* **10**, (2021).
508 16. Strom, A. R. *et al.* Phase separation drives heterochromatin domain formation. *Nature*
509 **547**, 241–245 (2017).
510 17. Sanulli, S. *et al.* HP1 reshapes nucleosome core to promote phase separation of
511 heterochromatin. *Nature* **575**, 390–394 (2019).
512 18. Holla, S. *et al.* Positioning Heterochromatin at the Nuclear Periphery Suppresses Histone
513 Turnover to Promote Epigenetic Inheritance. *Cell* **180**, 150-164.e15 (2020).
514 19. Fischer, T. *et al.* Diverse roles of HP1 proteins in heterochromatin assembly and
515 functions in fission yeast. *Proc Natl Acad Sci USA* **106**, 8998–9003 (2009).
516 20. Verschure, P. J. *et al.* In vivo HP1 targeting causes large-scale chromatin condensation
517 and enhanced histone lysine methylation. *Mol Cell Biol* **25**, 4552–64 (2005).
518 21. Keller, C. *et al.* HP1(Swi6) Mediates the Recognition and Destruction of
519 Heterochromatic RNA Transcripts. *Mol. Cell* **47**, 215–27 (2012).

520 22. Motamedi, M. R. *et al.* HP1 proteins form distinct complexes and mediate
521 heterochromatic gene silencing by nonoverlapping mechanisms. *Mol. Cell* **32**, 778–90 (2008).
522 23. Al-Sady, B., Madhani, H. D. & Narlikar, G. J. Division of labor between the
523 chromodomains of HP1 and Suv39 methylase enables coordination of heterochromatin
524 spread. *Mol. Cell* **51**, 80–91 (2013).
525 24. Akoury, E. *et al.* Disordered region of H3K9 methyltransferase Clr4 binds the
526 nucleosome and contributes to its activity. *Nucleic Acids Res* **47**, 6726–6736 (2019).
527 25. Canzio, D. *et al.* A conformational switch in HP1 releases auto-inhibition to drive
528 heterochromatin assembly. *Nature* **496**, 377–81 (2013).
529 26. Shirai, A. *et al.* Impact of nucleic acid and methylated H3K9 binding activities of
530 Suv39h1 on its heterochromatin assembly. *Elife* **6**, (2017).
531 27. Shimada, A. *et al.* Phosphorylation of Swi6/HP1 regulates transcriptional gene silencing
532 at heterochromatin. *Genes Dev* **23**, 18–23 (2009).
533 28. Eissenberg, J. C., Ge, Y. W. & Hartnett, T. Increased phosphorylation of HP1, a
534 heterochromatin-associated protein of Drosophila, is correlated with heterochromatin
535 assembly. *J. Biol. Chem.* **269**, 21315–21321 (1994).
536 29. LeRoy, G. *et al.* Heterochromatin Protein 1 Is Extensively Decorated with Histone Code-
537 like Post-translational Modifications*. *Mol. Cell. Proteomics* **8**, 2432–2442 (2009).
538 30. Nishibuchi, G. *et al.* N-terminal phosphorylation of HP1alpha increases its nucleosome-
539 binding specificity. *Nucleic Acids Res* **42**, 12498–511 (2014).
540 31. Zhao, T., Heyduk, T. & Eissenberg, J. C. Phosphorylation site mutations in
541 heterochromatin protein 1 (HP1) reduce or eliminate silencing activity. *J. Biol. Chem.* **276**,
542 9512–9518 (2001).

543 32. Greenstein, R. A. *et al.* Local chromatin context regulates the genetic requirements of the
544 heterochromatin spreading reaction. *PLoS Genet.* **18**, e1010201 (2022).
545 33. Greenstein, R. A. *et al.* Noncoding RNA-nucleated heterochromatin spreading is
546 intrinsically labile and requires accessory elements for epigenetic stability. *eLife* **7**, e32948
547 (2018).
548 34. O'Donoghue, L. & Smolenski, A. Analysis of protein phosphorylation using Phos-tag
549 gels. *J. Proteomics* **259**, 104558 (2022).
550 35. Jih, G. *et al.* Unique roles for histone H3K9me states in RNAi and heritable silencing of
551 transcription. *Nature* (2017) doi:10.1038/nature23267.
552 36. Yamada, T., Fischle, W., Sugiyama, T., Allis, C. D. & Grewal, S. I. S. The nucleation
553 and maintenance of heterochromatin by a histone deacetylase in fission yeast. *Mol. Cell* **20**,
554 173–85 (2005).
555 37. Cheutin, T., Gorski, S. A., May, K. M., Singh, P. B. & Misteli, T. In Vivo Dynamics of
556 Swi6 in Yeast: Evidence for a Stochastic Model of Heterochromatin. *Mol Cell Biol* **24**, 3157–
557 3167 (2004).
558 38. Hiragami-Hamada, K. *et al.* N-terminal phosphorylation of HP1{alpha} promotes its
559 chromatin binding. *Mol. Cell. Biol.* **31**, 1186–1200 (2011).
560 39. Williams, J. F. *et al.* The condensation of HP1-α/Swi6 imparts nuclear stiffness.
561 2020.07.02.184127 Preprint at https://doi.org/10.1101/2020.07.02.184127 (2023).
562 40. Biswas, S. *et al.* HP1 oligomerization compensates for low-affinity H3K9me recognition
563 and provides a tunable mechanism for heterochromatin-specific localization. *Sci. Adv.* **8**,
564 eabk0793 (2022).

565 41. Simon, M. D. *et al.* The site-specific installation of methyl-lysine analogs into
566 recombinant histones. *Cell* **128**, 1003–12 (2007).
567 42. Carpy, A. *et al.* Absolute proteome and phosphoproteome dynamics during the cell cycle
568 of Schizosaccharomyces pombe (Fission Yeast). *Mol. Cell. Proteomics MCP* **13**, 1925–1936
569 (2014).
570 43. Sadaie, M. *et al.* Balance between Distinct HP1 Family Proteins Controls
571 Heterochromatin Assembly in Fission Yeast. *Mol Cell Biol* **28**, 6973–6988 (2008).
572 44. Lemière, J., Real-Calderon, P., Holt, L. J., Fai, T. G. & Chang, F. Control of nuclear size
573 by osmotic forces in Schizosaccharomyces pombe. *eLife* **11**, e76075 (2022).
574 45. Neumann, F. R. & Nurse, P. Nuclear size control in fission yeast. *J Cell Biol* **179**, 593–
575 600 (2007).
576 46. Lantermann, A. B. *et al.* Schizosaccharomyces pombe genome-wide nucleosome
577 mapping reveals positioning mechanisms distinct from those of Saccharomyces cerevisiae.
578 *Nat Struct Mol Biol* **17**, 251-U15 (2010).
579 47. Godde, J. S. & Widom, J. CHROMATIN STRUCTURE OF
580 SCHIZOSACCHAROMYCES-POMBE - A NUCLEOSOME REPEAT LENGTH THAT IS
581 SHORTER THAN THE CHROMATOSOMAL DNA LENGTH. *J Mol Biol* **226**, 1009–1025
582 (1992).
583 48. Jarmoskaite, I., AlSadhan, I., Vaidyanathan, P. P. & Herschlag, D. How to measure and
584 evaluate binding affinities. *eLife* **9**, e57264 (2020).
585 49. Hou, H. *et al.* Csi1 links centromeres to the nuclear envelope for centromere clustering. *J.*
586 *Cell Biol.* **199**, 735–744 (2012).

587 50. Barrales, R. R., Forn, M., Georgescu, P. R., Sarkadi, Z. & Braun, S. Control of
588 heterochromatin localization and silencing by the nuclear membrane protein Lem2. *Genes*
589 *Dev* **30**, 133–48 (2016).
590 51. Al-Sady, B., Greenstein, R. A., El-Samad, H. J., Braun, S. & Madhani, H. D. Sensitive
591 and Quantitative Three-Color Protein Imaging in Fission Yeast Using Spectrally Diverse,
592 Recoded Fluorescent Proteins with Experimentally-Characterized In Vivo Maturation
593 Kinetics. *PLoS One* **11**, e0159292 (2016).
594 52. Zhao, T. & Eissenberg, J. C. Phosphorylation of heterochromatin protein 1 by casein
595 kinase II is required for efficient heterochromatin binding in Drosophila. *J. Biol. Chem.* **274**,
596 15095–15100 (1999).
597 53. Nishibuchi, G. *et al.* Mitotic phosphorylation of HP1α regulates its cell cycle-dependent
598 chromatin binding. *J. Biochem. (Tokyo)* **165**, 433–446 (2019).
599 54. Sokolova, V. *et al.* Structural mechanism of HP1α-dependent transcriptional repression
600 and chromatin compaction. *Struct. Lond. Engl. 1993* S0969-2126(24)00382–4 (2024)
601 doi:10.1016/j.str.2024.09.013.
602 55. Murawska, M. *et al.* The histone chaperone FACT facilitates heterochromatin spreading
603 by regulating histone turnover and H3K9 methylation states. *Cell Rep.* **37**, 109944 (2021).
604 56. Cutter DiPiazza, A. R. *et al.* Spreading and epigenetic inheritance of heterochromatin
605 require a critical density of histone H3 lysine 9 tri-methylation. *Proc. Natl. Acad. Sci. U. S. A.*
606 **118**, e2100699118 (2021).
607 57. Iglesias, N. *et al.* Native Chromatin Proteomics Reveals a Role for Specific Nucleoporins
608 in Heterochromatin Organization and Maintenance. *Mol. Cell* **77**, 51-66.e8 (2020).

609 58. Stirpe, A. *et al.* SUV39 SET domains mediate crosstalk of heterochromatic histone
610 marks. *eLife* **10**, e62682 (2021).
611 59. Zofall, M., Sandhu, R., Holla, S., Wheeler, D. & Grewal, S. I. S. Histone deacetylation
612 primes self-propagation of heterochromatin domains to promote epigenetic inheritance. *Nat.*
613 *Struct. Mol. Biol.* **29**, 898–909 (2022).
614 60. Dong, W. *et al.* Abo1 is required for the H3K9me2 to H3K9me3 transition in
615 heterochromatin. *Sci. Rep.* **10**, 6055 (2020).
616 61. Torres-Garcia, S. *et al.* SpEDIT: A fast and efficient CRISPR/Cas9 method for fission
617 yeast. *Wellcome Open Res.* **5**, 274 (2020).
618 62. Rougemaille, M., Shankar, S., Braun, S., Rowley, M. & Madhani, H. D. Ers1, a rapidly
619 diverging protein essential for RNA interference-dependent heterochromatic silencing in
620 Schizosaccharomyces pombe. *J. Biol. Chem.* **283**, 25770–25773 (2008).
621 63. Bolger, A. M., Lohse, M. & Usadel, B. Trimmomatic: a flexible trimmer for Illumina
622 sequence data. *Bioinforma. Oxf. Engl.* **30**, 2114–2120 (2014).
623 64. Langmead, B. & Salzberg, S. L. Fast gapped-read alignment with Bowtie 2. *Nat. Methods*
624 **9**, 357–359 (2012).
625 65. Li, H. *et al.* The sequence alignment/map format and SAMtools. *Bioinformatics* **25**,
626 2078–2079 (2009).
627 66. Ramírez, F., Dündar, F., Diehl, S., Grüning, B. A. & Manke, T. DeepTools: A flexible
628 platform for exploring deep-sequencing data. *Nucleic Acids Res* **42**, W187–W191 (2014).
629 67. Lawrence, M., Gentleman, R. & Carey, V. rtracklayer: an R package for interfacing with
630 genome browsers. *Bioinforma. Oxf. Engl.* **25**, 1841–1842 (2009).

631 68. Hahne, F. & Ivanek, R. Visualizing Genomic Data Using Gviz and Bioconductor.
632 *Methods Mol. Biol. Clifton NJ* **1418**, 335–351 (2016).
633 69. GenomicRanges. *Bioconductor* http://bioconductor.org/packages/GenomicRanges/.
634 70. Edelstein, A. D. *et al.* Advanced methods of microscope control using μManager
635 software. *J. Biol. Methods* **1**, e10 (2014).
636 71. Edelstein, A., Amodaj, N., Hoover, K., Vale, R. & Stuurman, N. Computer control of
637 microscopes using μManager. *Curr. Protoc. Mol. Biol.* **Chapter 14**, Unit14.20 (2010).
638 72. Ershov, D. *et al.* TrackMate 7: integrating state-of-the-art segmentation algorithms into
639 tracking pipelines. *Nat. Methods* **19**, 829–832 (2022).
640 73. Tinevez, J.-Y. *et al.* TrackMate: An open and extensible platform for single-particle
641 tracking. *Methods San Diego Calif* **115**, 80–90 (2017).
642 74. Liu, H., Lin, D. & Yates, J. R. Multidimensional separations for protein/peptide analysis
643 in the post-genomic era. *BioTechniques* **32**, 898, 900, 902 passim (2002).
644 75. Washburn, M. P., Wolters, D. & Yates, J. R. Large-scale analysis of the yeast proteome
645 by multidimensional protein identification technology. *Nat. Biotechnol.* **19**, 242–247 (2001).
646
647
648
649
650
651
652
653
654
655

Acknowledgments

We would like to thank Geeta J. Narlikar for the discussion on theory and critical feedback on the manuscript. We thank Sigurd Braun, Daniele Canzio, and Lucy D. Brennan for valuable feedback and discussion. B.A-S. was supported by a National Institutes of Health grant R35GM141888 and a National Science Foundation grant 2113319. D.R.K. and C.T. were supported by a National Science Foundation Graduate Research Fellowships Grant No. 2034836. E.S. was supported by a grant from the Ford Foundation and National Institutes of Health supplement DP2GM123484-01S1. We acknowledge the UCSF PFCC (RRID:SCR_018206) for assistance in generating Flow Cytometry data. The research reported here was supported in part by the DRC Center Grant NIH P30 DK063720. We thank the Southworth lab for access and training to SEC-MALS equipment.

667 **FIGURE LEGENDS**

668 **Figure 1: S18 and S24 in Swi6 are required for spreading, but not nucleation of**
669 **heterochromatin silencing. A.** Overview of the Swi6 protein domain architecture and previously
670 identified (Shimada *et al.*) *in vivo* phosphorylation sites (green residue numbers). NTE: N-terminal
671 extension; CD: chromodomain (H3K9me binding); HINGE: unstructured hinge region; CSD:
672 chromo-shadow domain (dimerization and effector recruitment). **B.** Strategy for production of *swi6*
673 S-A mutants in the MAT *ΔREIII* HSS reporter background. **C.** Swi6 levels are not affected by S-A
674 mutations. Total extracts of *swi6* wild-type or indicated mutants were probed with an anti-Swi6
675 polyclonal antibody. *In vitro* purified Swi6 that was either phosphorylated (pSwi6) or not (unpSwi6)
676 is run as size controls. Note, not all mutant Swi6 proteins display a band shift even if they retain
677 phosphosites **D.-I.** 2-D Density hexbin plots examining silencing at nucleation "green" and
678 spreading "orange" reporter in *Δswi6,* wild-type, and indicated S-A mutants. The yellow box
679 indicates a "green" and "orange" regime consistent with silencing loss, and the magenta box
680 indicates a regime consistent with loss of spreading, but not nucleation. The dashed line indicates
681 the threshold for orange ON and the numbers the fraction of cells above the line.

682

683 **Figure 2: Conversion from H3K9me2 to H3K9me3 is compromised outside nucleation**
684 **centers in S18 and S24 Swi6 mutants. A.** Overview of the ChIP-seq experiments. **B-D.** ChIP-
685 seq signal visualization plots. The solid ChIP/input line for each genotype represents the mean of
686 three repeats, while the shading represents the 95% confidence interval. **B.** Plots of H3K9me2
687 (TOP) and H3K9me3 (BOTTOM) ChIP signal over input at the MAT *ΔREIII* HSS mating type locus
688 for wild-type (black), *swi6*$^{S18/24A}$ (blue), and *Δswi6* (gold). Signal over "green" and "orange"
689 reporters are greyed out, as reads from these reporters map to multiple locations within the
690 reference sequence, as all reporters contain control elements derived from the *ura4* and *ade6*
691 genes. **C.** H3K9me2 (TOP) and H3K9me3 (BOTTOM) plots as in A. for subtelomere IIR for wild-
692 type and *swi6*$^{S18/24A}$. The red bar on the H3K9me2 plots indicates the distance from *tlh2* to where
693 H3K9me2 levels drop in *swi6*$^{S18/24A}$ relative to wild-type. Inset: a zoomed-in view proximal to *tlh2*
694 is shown for H3K9me2 and me3. The red arrows in the insets indicate the point of separation of
695 the 95% confidence intervals, which is significantly further telomere proximal for H3K9me3. **D.**
696 H3K9me2 (TOP) and H3K9me3 (BOTTOM) plots as in A. for centromere II for wild-type and
697 *swi6*$^{S18/24A}$. Inset: the left side of the pericentromere.

698

699 **Figure 3: Swi6 phosphorylation increases oligomerization and decreases nucleosome**
700 **binding, without affecting specificity. A.** Production of phosphorylated Swi6 (pSwi6) in *E. coli.*
701 Casein Kinase II (CKII) is co-expressed with Swi6. After lysis and purification, the 6X His tag is
702 removed from the pSwi6 or unpSwi6 protein. **B.** Mass Spectrometry on pSwi6. Shown is a domain
703 diagram of Swi6. Phosphorylation sites identified in pSwi6 by 2D-ETD-MS are indicated and
704 grouped by detection prevalence in the sample. **C.** Size Exclusion Chromatography followed by
705 Multi-Angle Light Scattering (SEC-MALS) on EDC/NHS cross-linked unpSwi6 (black) and pSwi6
706 (green). Relative refractive index signals (solid lines, left y-axis) and derived molar masses (lines
707 over particular species, right y-axis) are shown as a function of the elution volume. [Swi6] was
708 100μM. **D.** Fluorescence polarization (FP) with fluorescein (star)- labeled H3 tail peptides (1-20)
709 and pSwi6 (green) or unpSwi6 (black) for H3K9me0 (open circles) and H3K9me3 (filled circles)
710 is shown. Error bars represent standard deviation. Binding was too low to be fit for unpSwi6 and
711 H3K9me0 peptides. **E.** FP with H3K9me0 (open circles) or $H3K_c9me3$ (MLA, filled circles)
712 mononucleosomes. Fluorescein (green star) is attached by a flexible linker at one end of the 147
713 bp DNA template. For D.&E., the average of three independent fluorescent polarization
714 experiments for each substrate is shown. Error bars represent standard deviation. **F.** Summary
715 table of affinities and specificities for D. and E. **G.** Representative maximum projection live
716 microscopy images of indicated Swi6-GFP / Sad1-mKO2 strains. **H.** Analysis of signal intensity in
717 Swi6-GFP foci in indicated strains. Wt Swi6, n=242; $Swi6^{S18/24A}$, n=251; $Swi6^{S18/24/117-220A}$, n=145;
718 $Swi6^{S46/52/117-220A}$, n=192. n, number of foci analyzed.

719

720 **Figure 4: Swi6 phosphorylation mitigates inhibition of the Clr4-mediated conversion of**
721 **H3K9me2 to H3K9me3 A.** Most Swi6 molecules in the cell are phosphorylated at S18 and S24.
722 Quantitative western blots against total Swi6 and phosphorylated Swi6 at S18/S24. A standard
723 curve of pSwi6 isolated as in Figure 3 is included in both blots. Total protein lysates from wild-
724 type *swi6* and $swi6^{S18/24A}$ strains were probed with a polyclonal anti-Swi6 antibody (α-Swi6) or an
725 antibody raised against a phosphorylated S18/S24 peptide (α-S18P-S24P). α-tubulin was used
726 as a loading control. One of two independent experiments is shown. L; ladder. **B.** Experimental
727 scheme to probe the impact of Swi6 on H3K9 trimethylation. **C.** Quantitative western blots on the
728 time-dependent formation of H3K9me3 from H3K9me2 mononucleosomes in the presence of
729 pSwi6 or unpSwi6. The same blots were probed with α-H3K9me3 and α-H4 antibodies as a
730 loading and normalization control. **D.** Single exponential fits of production of H3K9me3 tails over
731 time for indicated concentrations of unpSwi6 or pSwi6. **E.** plot of k_{obs} vs. [Swi6] (μM). **F.**

732 Fluorescence polarization with H3K9me0 (open circles) or H3K$_c$9me3 (MLA, filled circles)
733 mononucleosomes as in Figure 3E., with pSwi6 (green) or pSwi6$^{S18/24A}$ (magenta). Relative K_d
734 values in Table 1. Error bars represent standard deviation. **G.** Model of the impact of pSwi6 on
735 Clr4 activity. Top: pSwi6 does not engage with K3K9me0 nucleosomes, clearing the substrate for
736 Clr4, and has reduced interactions with the nucleosome core. Bottom: Swi6 binds H3K9me3 and
737 me0 nucleosomes, occluding Clr4 access.

738 **Table 1.** Relative affinities of pSwi6 and pSwi6$^{S18/24A}$ for H3K9me0 and H3K9me3 nucleosomes.

739 **Table 2.** Table of *S. pombe* strains used in this work.

740

741 **Supporting Figure 1: Additional isolates demonstrating that S18 and S24 in Swi6 are**
742 **required for spreading, but not nucleation of heterochromatin silencing.** 2-D Density hexbin
743 plots examining silencing at nucleation "green" and spreading "orange" reporter in the MAT *ΔREIII*
744 HSS for three additional isolates of **A.-C.** *swi6*$^{S18/24A}$ mutants, **C.-F.** *swi6*$^{S46/5/117-220A}$ ("S18/24
745 available"), and **G.-I.** *swi6*$^{S46/52A}$. **J-L.** As A.-I. but for the *Δckb1* mutant. An independent wild-type
746 isolate from the cross is shown alongside 2 *Δckb1* isolates.

747 **Supporting Figure 2: H3K9me2 and H3K9me3 ChIP-seq plots in additional genomic loci in**
748 **wild-type or *swi6*$^{S18/24A}$ A.** H3K9me2 (TOP) and H3K9me3 (BOTTOM) plots as in Figure 2 at
749 *mei4* for wild-type and *swi6*$^{S18/24A}$. **B.** H3K9me2 (TOP) and H3K9me3 (BOTTOM) plots as in
750 Figure 2 at *tel IL* for wild-type and *swi6*$^{S18/24A}$. **B.** H3K9me2 (TOP) and H3K9me3 (BOTTOM) plots
751 as in Figure 2 at *tel IIL* for wild-type and *swi6*$^{S18/24A}$.

752 **Supporting Figure 3: Characterization of recombinant pSwi6 A.** Size Exclusion
753 Chromatography followed by Multi-Angle Light Scattering (SEC-MALS) on uncrosslinked
754 unpSwi6 (black) and pSwi6 (green). Relative refractive index signals (solid lines, left y-axis) and
755 derived molar masses (lines over particular species, right y-axis) are shown as a function of the
756 elution volume. A migration shift is apparent in pSwi6, as well as a small shoulder of higher
757 molecular weight species (arrow). **B.** Calf Intestine Phosphatase (CIP) treatment of Swi6
758 examined in a 15% SDS-PAGE gel. unpSwi6, pSwi6, or pSwi6$^{S18/24A}$ were treated with (+) or
759 without (-) CIP or with heat-inactivated CIP (b). **C.** CIP treatment of Swi6 examined in a Phos-Tag
760 gel as in A. Blots of both gels were probed with an anti-Swi6 polyclonal antibody. **D.** Mass
761 Spectrometry on pSwi6$^{S18/24A}$. Shown is a domain diagram of Swi6$^{S18/24A}$. Phosphorylation sites

762 identified in pSwi6 $^{S18/24A}$ by 2D-ETD-MS are indicated and grouped by detection prevalence in
763 the sample.

764 **Supporting Figure 4: Analysis of Swi6-GFP heterochromatin foci number and spatial**
765 **distribution. A.** Strategy for production of GFP-tagged *swi6* S-A mutants in the *sad1:mKO2*
766 background. The wildtype *swi6* or S-A mutant gene from Figure 2A was cut with CRISPR/Cas9,
767 and the break was repaired with a cassette containing a super-folder GFP, *swi6* 3' sequence
768 homology, and a HygMX cassette. **B.** Representative maximum projection live microscopy
769 images of indicated Swi6$^{S46/52A}$-GFP /Sad1-mKO2 compared to the wild-type strain. **C.**
770 Quantification of Swi6-GFP signals by flow cytometry. The GFP signal of independent wild-type
771 or S-A mutant isolates compared to GFP- cells as measured by flow cytometry. **D.** Distribution of
772 nuclear foci in nuclei of indicated strains represented as relative frequency. Wt Swi6-GFP , n=85;
773 Swi6$^{S18/24A}$-GFP, n=94; Swi6$^{S18/24/117-220A}$-GFP, n=50; Swi6$^{S46/52/117-220A}$-GFP, n=82. **E.** distribution
774 of Swi6-GFP heterochromatin foci relative to Sad1-mKO2. overview: center-to-center distances
775 were measured in 3D from the peri-spindle pole body Sad1-mKO2 signal to all Swi6-GFP foci
776 identified in each nucleus. **F.** relative frequency histogram binning the distribution of Sad1-mKO2
777 to Swi6-GFP foci distances in indicated strains.

778 **Supporting Figure 5: Additional replicates of Swi6 westerns from cell lysates and**
779 **nucleosome trimethylation. A.** Independent repeat of α-Swi6 and α-S18P-S24P westerns as
780 in Figure 4A. **B.** A repeat of quantitative western blots querying time-dependent formation of
781 H3K9me3 from H3K9me2 mononucleosomes in the presence of pSwi6 or unpSwi6 (0 and 5μM
782 Swi6). **C.** A repeat of quantitative western blots querying time-dependent formation of H3K9me3
783 from H3K9me2 mononucleosomes in the presence of pSwi6 or unpSwi6 (15μM and 30μM Swi6).
784 B and C. Swi6 concentration time courses were collected at the same time; westerns were run on
785 separate days.

786

787 **METHODS**

788

789 *Strain construction*

790 To construct wild-type *swi6* and *swi6* phosphoserine mutants, the swi6 open reading frame
791 (ORF) was first deleted by integrating a *ura4* gene cassette in the MAT HSS background. A
792 plasmid, pRS316, was constructed containing 5' homology-*swi6* promoter-*swi6 (or swi6* S-A
793 mutant*)*- 3' UTR-*kan*-3' genome homology and linearized by PmeI double digest to replace the
794 *ura4* cassette by genomic integration via homologous recombination. After transformation, cells
795 were plated on YES agar for 24 hours before replica plating on G418 selection plates. For the
796 Δ*ckb1* mutant, we crossed the deletion strain from our chromatin function library[32] to the MAT
797 ΔREIII HSS and selected Δ*ckb1* MAT ΔREIII HSS strains by random spore analysis on
798 HYG+G418 double selection. For Swi6-GFP fusions in the Sad1-mKO2 background, *swi6* wild-
799 type and *swi6* S-A mutant strains were first crossed with the *sad1::mkO2* strain to remove the
800 MAT HSS. Next, *swi6* and *swi6* S-A mutant ORFs were C-terminally fused to SF-GFP followed
801 by a hygromycin resistance marker by CRISPR/Cas9 editing as previously described[61].
802 Modifications were confirmed by gDNA extraction and PCR amplification of the 5' *swi6* to 3'
803 genome region downstream from the hygromycin marker. For all strain construction, isolates
804 were verified by genomic PCR.

805

806 *Western blot*

807 Proteins were separated on a 15% SDS-Page gel and transferred to a PVDF membrane
808 (Millipore) for 90 minutes at 100V and 4°C. Membranes were blocked overnight in 1:1 1X PBS:
809 Intercept PBS Blocking Buffer (LiCor). Next, membranes were incubated with either polyclonal
810 anti-Swi6 antibody[25] or anti-pSwi6 antibody (Rockland Immunochemicals, this study) diluted
811 1:1000 in 1:1 1X PBS, 0.2% Tween-20 (PBS-T): Intercept PBS Blocking Buffer overnight at 4°C
812 on a nutator. Anti-α-tubulin antibody was diluted 1:2000 and used as loading control.
813 Membranes were washed twice with PBS-T for 10 minutes followed by two washes for 5
814 minutes before incubation with secondary antibodies. Secondary fluorescent antibodies were
815 diluted either 1:10000 (anti-rabbit, 680 nm, Cell Signaling Technology 5366P, lot # 14) or 1:5000
816 (anti-mouse, 800 nm, Li-Cor, D10603-05) and were incubated with the membranes for 45
817 minutes at RT. Finally, membranes were washed 3 times with PBS-T for 10 minutes and once
818 with PBS for 10 minutes before imaging on a LiCor Odyssey CLx imager.

819

820 *HSS Flow cytometry*

821 Strains were struck out of a -80°C freezer onto YES plates. Recovered cells were grown in 200
822 μL of YES media in a 96-well plate overnight to saturation at 32°C. The next morning, cells were
823 diluted 1:25 in YES media into mid-log phase and analyzed by flow cytometry on an LSR
824 Fortessa X50 (BD Biosciences). Fluorescence compensation, data analysis, and plotting in R
825 were performed as described in Greenstein *et al.* 2022[33].
826
827 *Chromatin immunoprecipitation followed by sequencing (ChIP -seq) sample collection and*
828 *library preparation*
829 Cells were grown in YES media overnight to saturation (32°C, 225RPM shaking). The following
830 morning cells were diluted to OD 0.03, grown to OD 1, and $300x10^6$ were fixed and frozen at -
831 80°C. Cells were processed for ChIP as described in Canzio *et al.* 2011 with the following
832 modifications: Three technical replicates were processed for ChIP-seq. After lysis, cells were
833 bead beat 10 rounds for 1 minute each round with 0.5 mm Zirconia/Silica beads (Cat No.
834 11079105z). Tubes were chilled on ice for 2 minutes between rounds. Lysates were then spun
835 down to isolate chromatin. The chromatin pellet was resuspended in 1.5 mL lysis buffer, moved
836 to a 15 mL Diagenode Bioruptor tube (Cat. No. C01020031) and sonicated with a Diagenode
837 Bioruptor Pico sonicator for a total of 35 cycles, 30 seconds on/ 30 seconds off, in the presence
838 of sonication beads (Diagenode, Cat. No. C03070001). Every 10 cycles tubes were vortexed.
839 Chromatin lysate was spun down for 30 minutes at 14000 RPM and 4°C. The lysate volume
840 was brought up to 900 μL. 45 μL was taken out to check shearing of the DNA. 40 μL was taken
841 out for input and kept at RT until the reverse crosslinking step. The remaining ~800 μL was
842 divided into 2 tubes to incubate with either 2 μL anti-H3K9me2 (Abcam 1120, Lot No. 1009758-
843 6) or 1 μg anti-H3K9me3 (Diagenode, Cat. No. C15500003 Lot No. 003) overnight on a tube
844 rotator at 4°C. The next morning, Protein A Dynabeads (Invitrogen, LOT 01102248) and M280
845 Streptavidin beads (Invitrogen, LOT 2692541) were washed twice with Lysis Buffer without
846 protease inhibitors. 20 μL Protein A Dynabeads beads were added to each anti-H3K9me2
847 sample, and 30 μL M-280 Streptavidin beads were added to each anti-H3K9me3 sample.
848 Beads were incubated with samples for 3 hours on a tube rotator at 4°C, and then washed with
849 700 μL cold buffers at RT on a tube rotator in the following order: 2X Lysis Buffer for 5 minutes,
850 2X High Salt Buffer for 5 minutes, 1X Wash Buffer for 5 minutes, and 1X TE (buffer recipes as
851 in[62]). Samples were incubated with 100 μL elution buffer (50 mM Tris pH 8.0, 10 mM EDTA,
852 1% SDS) for 20 minutes at 70°C in a ThermoMixer F1.5 (Eppendorf). Input samples were
853 brought up to 100 μL in TE with a final concentration of 1% SDS. Input and eluted samples were

854 then incubated overnight in a 65°C water bath with 2.5 µL 2.5 mg/mL Proteinase K (Sigma
855 Aldrich, Lot 58780500) for reverse crosslinking. Samples were purified with a PCR clean-up kit
856 (Machery-Nagel) and eluted in 100 µL 10 mM Tris pH 8.0. The quality and size of the DNA were
857 assessed by 4200 TapeStation instrument (Agilent). Next, libraries were prepared using Index
858 Primer Set 1 (NEBNext Multiplex Oligos for Illumina, E7335L, Lot 10172541), Ultra II FS DNA
859 Library Prep Kit for Illumina (E7805L, Lot 10202083). The manufacturer's protocol, "Protocol for
860 FS DNA Library Prep Kit (E7805, E6177) with Inputs ≤100 ng (NEB)", was used starting with
861 200 pg of DNA. PCR-enriched adaptor-ligated DNA was cleaned up using NEBNext sample
862 purification beads (E6178S, Lot 10185312, "1.5. Cleanup of PCR Reaction" in manufacturer's
863 protocol). Individual adaptor-ligated DNA sample concentrations were quantified using a Qubit 4
864 Fluorometer (Thermo Fisher), and the quality of the DNA was assessed by a 4200 TapeStation
865 instrument (Agilent). Libraries were pooled to equimolar quantities and sequenced using a
866 NextSeq 2000 P2 (400 million clusters) (Chan Zuckerberg Biohub San Francisco) (40bp read
867 length, paired-end).
868
869 *ChIP-seq data analysis*
870 Sequencing adaptors were trimmed from raw sequencing reads using Trimmomatic v0.39.
871 The S. pombe genome was downloaded from NCBI under Genome Assembly ASM294v2. The
872 MAT locus of chromosome II was edited to our custom HSS MAT locus, and the genome was
873 indexed using the bowtie2-build function of Bowtie2 v2.5.1[63]. Trimmed sequencing reads were
874 aligned to the genome using Bowtie2 v2.5.1 with flags [--local --very-sensitive-local --no-unal --
875 no-mixed --no-discordant --phred33 -I 10 -X 700][64]. Next, the resulting SAM files were converted
876 to BAM files using SAMtools v1.18[65] view function: -S -b ${base}.sam > ${base}.bam. The
877 resulting BAM files were further processed by removing low-quality alignments, PCR duplicates,
878 and multimappers, and retain properly aligned paired-end reads using SAMtools view with the
879 following flags: -bh -F 3844 -f 3 -q 10 -@ 4. The processed BAM files were then sorted and
880 indexed (SAMtools). Sorted, indexed BAM files were converted to bigWig coverage tracks using
881 deepTools v3.5.4[66]: bamCoverage: -b "$bam_file" -o "$filename_without_extension.bw" --
882 binSize 10 --normalizeUsing CPM --extendReads --exactScaling --samFlagInclude 64 --
883 effectiveGenomeSize 13000000. BigWig files normalized to input were generated using the
884 bigwigCompare tool (deepTools). Normalized bigWig files were loaded into R v4.3.0 using
885 rtracklayer v1.60.1[67] and processed for visualization as in Greenstein *et al.* 2022 with
886 modifications. The Gviz v1.44.2 (Bioconductor) DataTrack function was used to create a
887 visualization track of ChIP-seq signal in bigWig files for each genotype[68]. The Bioconductor

888 GenomicRanges package was used to create a GRanges object to store custom genomic
889 coordinates defined by a BEDfile[69]. Genomic annotations for signal tracks were created using
890 the AnnotationTrack (Gviz) function. The GenomeAxisTrack (Gviz) function generated a visual
891 reference (in megabases) to display the position of genomic annotations and signal tracks.
892 Finally, the plotTracks (Gviz) function was used to plot the DataTrack, AnnotationTrack, and
893 GenomeAxisTrack objects for visualization.
894
895 *Swi6-GFP live cell imaging*
896 Swi6-GFP/Sad1-mKO2 strains were struck out onto fresh YES 225 agar plates and incubated at
897 32°C for 3-5 days. Colonies were inoculated into liquid YES 225 medium (#2011, Sunrise
898 Science Production) and grown in an incubator shaker at 30°C, 250 rpm to an OD of 0.2 -0.6.
899 Cells were placed onto 2% agarose (#16500500, Invitrogen) pads in YES 225, covered with a
900 coverslip (#2850-22, thickness 1 ½, Corning), and sealed with VALAP for imaging. Cells were
901 imaged on a Ti-Eclipse inverted microscope (Nikon Instruments) with a spinning-disk confocal
902 system (Yokogawa CSU-10) and a Borealis illumination system that includes 488nm and 541nm
903 laser illumination and emission filters 525±25nm and 600±25nm respectively, 60X (NA: 1.4)
904 objectives, and an EM-CCD camera (Hamamatsu, C9100-13). These components were
905 controlled with μManager v. 1.41[70,71]. The temperature of the sample was maintained at 30°C by
906 a black panel cage incubation system (#748–3040, OkoLab). The middle plane of cells was first
907 imaged in brightfield and then two Z-stacks with a step size of 0.5μm were acquired in spinning-
908 disk confocal mode with laser illumination 488nm and 541nm (total of 9 imaging planes per
909 channel). The exposure, laser power, and EM gain for the Z-stacks were respectively 50ms /
910 1% / 800, and 200ms / 5% / 800. Between 9 and 12 fields of view were acquired per strain.
911
912 *Image analysis*
913 For each field of view, nuclei were manually cropped using Fiji. Cells containing multiple Sad1-
914 mK02 foci were discarded from this analysis. For each selected nucleus TrackMate was used to
915 determine the coordinates in space (X, Y, Z) of Sad1 and every Swi6 focus and their
916 fluorescence intensity[72,73]. Using a custom script on Jupiter Notebook in Python we then
917 automatically counted the number of Swi6 foci detected by TrackMate for each nucleus.
918 Additionally, we automated the calculation of the distance between Swi6 foci and the spindle
919 pole body by measuring the distance from each Swi6 focus to Sad1 within a given nucleus. For
920 Swi6 intensity measurements, a region of interest (ROI) outside of each nucleus was
921 automatically selected to measure the background intensity. This background intensity was then

922 used to correct Swi6 fluorescence signal by subtracting the average intensity of this ROI for a
923 given analyzed nucleus. Finally, we used a one-way ANOVA statistical test on Swi6 intensity
924 signal to determine differences between mutants.
925
926 *Protein cloning and purification*
927 Wildtype *swi6* open reading frame was cloned by ligation-independent cloning into vector 14B
928 (QB3 Berkeley Macrolab expression vectors). Vector 14B encodes an N-terminal 6xHis tag
929 followed by a TEV cleavage sequence. Wildtype Swi6 was expressed in BL21-gold (DE3)
930 competent cells. To produce $Swi6^{S18/24A}$, a gene block containing S18A/S24A Swi6 was cloned
931 into vector 14B using Gibson assembly. To isolate pSwi6 and $pSwi6^{S18/S24A}$, the respective
932 vectors were co-expressed with the catalytic subunits of Caesin Kinase II in pRSFDuet. All three
933 proteins were grown, harvested, and purified using a protocol adapted from [10] and modified as
934 follows: Cells were grown at 37°C until OD600 0.5-0.6 and induced with a final concentration of
935 0.4mM Isopropyl-β-D-thiogalactopyranoside. Induced cells were grown at 18°C overnight.
936 Harvested cells were resuspended in lysis buffer containing 1X PBS buffer pH 7.3, 300 mM
937 NaCl, 10% glycerol, 0.1% Igepal CA-630, 7.5 mM Imidazole, 1 mM Beta-Mercaptoethanol
938 (βME), with protease inhibitors. Resuspended cells were sonicated 2 seconds on /2 seconds off
939 at 40% output power for three 5-minute cycles. The lysate was centrifuged at 25,000xg for 25
940 minutes, and the supernatant was collected. Nickel NTA resin was equilibrated with lysis buffer.
941 The supernatant and resin were incubated for 1-2 hours and washed 3 times with 40 ml of lysis
942 buffer each time before the protein was eluted with 25 mM HEPES pH 7.5, 100 mM KCl, 10%
943 glycerol, 400 mM Imidazole, and 1 mM βME. The eluted protein was then dialyzed in TEV
944 cleavage buffer containing 25 mM HEPES pH 7.5, 100 mM KCl, and 1 mM βME and 6 mg TEV
945 protease. The following morning 3-6 mg of TEV protease was spiked in for about 1 hour to
946 ensure full cleavage. Nickel NTA resin was equilibrated with TEV cleavage buffer and the his-
947 tagged TEV was captured by the resin while Swi6 protein was isolated by gravity flow. Cleaved
948 protein was concentrated using a 10kDa MWCO concentrator and applied to a Superdex 200
949 Increase 10/300 GL size exclusion column equilibrated in storage buffer containing 25 mM
950 HEPES pH 7.5, 100 mM KCl, 10% glycerol, and 10 mM βME. Protein was concentrated, flash-
951 frozen in N_2 (liq), and stored at -80°C. Protein concentration was quantified against a BSA
952 standard curve on an SDS page gel and sypro red stain.
953
954
955

956 *EDC/NHS crosslinking*
957 unpSwi6 or pSwi6 was purified as described above. However, the storage buffer was 25 mM
958 HEPES pH 7.5 and 100 mM KCl for SEC-MALS. Protein, either 100 µM Swi6 or pSwi6, was
959 incubated with 2 mM EDC and 5 mM NHS in a total volume of 95 µL for 2 hours. The reaction
960 was quenched with a final concentration of 20 mM hydroxylamine.
961
962 *Size-exclusion Chromatography coupled with Multi-Angle Light Scattering (SEC-MALS)*
963 Crosslinked and uncrosslinked Swi6 and pSwi6 were filtered with 0.2 µm spin columns (Pall
964 Corporation, Ref. ODM02C34). For SEC, uncrosslinked and crosslinked proteins were injected
965 onto a KW-804 silica gel chromatography column (Shodex) in a volume of 50 µL at 100 µM. The
966 column was run using an ÄKTA pure FPLC (GE Healthcare Life Sciences) and equilibrated with
967 SEC-MALS storage buffer at a flow rate of 0.4 mL/min and temperature of 8°C. The SEC
968 column was connected in-line to a DAWN HELEOS II (Wyatt Technology) 18-angle light
969 scattering instrument and an Optilab T-rEX differential refractive index detector (Wyatt
970 Technology). Data was analyzed using ASTRA software (version 7.1.4.8, Wyatt Technology)
971 and graphed using GraphPad Prism software (version 9.5.1).
972
973 *Fluorescence Polarization*
974 Fluorescence Polarization binding measurements were conducted as described in Canzio *et al.*
975 2013 and modified as follows:
976 Peptide reaction buffer was 50 mM HEPES pH 7.5, 100 mM KCl, 10% glycerol, 0.01% NP-40,
977 and 2 mM βME. Fluoresceinated $H3_{1–20}$ K9me0 or $H3_{1–20}$ K9me3 peptide concentration was
978 fixed at 100 nM while Swi6, pSwi6, or $pSwi6^{S18/24A}$ protein concentration varied from 0-200 µM.
979 Mononuclesome reaction buffer was 20 mM HEPES pH 7.5, 80 mM KCl, 4 mM Tris, 0.2 mM
980 EDTA, 10% glycerol, 0.01% NP-40, 2 mM βME. H3K9me0 and $H3K_C9me3$ mononucleosomes
981 were reconstituted with fluorescein-labeled 601 DNA as described[12]. Nucleosome concentration
982 was fixed at 25 nM while Swi6, pSwi6, or $pSwi6^{S18/24A}$ protein concentrations varied from 0-200
983 µM. Both peptide and mononucleosome reaction volumes were 10 µL and measured in a
984 Corning 384 low-volume, flat bottom plates (product number 3820, LOT 23319016).
985 Fluorescence polarization was recorded using a Cytation 5 microplate reader (Biotek, λ_{ex}=
986 485/20nm, λ_{em}= 528/20nm) and Gen5 software (Biotek, version 3.09.07). Data was analyzed
987 and fit to a K_d equation using GraphPad Prism.
988
989

990

991 *Single turnover kinetics*

992 Clr4 protein was purified exactly as described[23]. H3K9me2 nucleosomes were purchased from
993 Epicypher (#16-0324), and pSwi6 and unpSwi6 were purified as above. Single turnover
994 reactions were carried out as follows: 5 μM Clr4 was preincubated 5 minutes with 1 mM final S-
995 adenosyl-methionine (liquid SAM, 3 2mM, NEB #B9003S), and varying concentrations of pSwi6
996 or unP Swi6, at 25°C to reach equilibrium. 5μM Clr4 was chosen as the minimal Clr4
997 concentration to yield robust H3K9me3 signal under Single Turnover conditions. The reaction
998 was started with the addition of H3K9me2 nucleosomes to 500nM final. Timepoints were
999 stopped by boiling with SDS-Laemmli buffer. Samples were separated on 18% SDS-PAGE gel
1000 and probed for the presence of H3K9me3 (polyclonal, Active Motif #39161. lot 22355218-11)
1001 and H4 (Active Motif #39269 lot 31519002) as a loading control. Signals were quantified on a Li-
1002 Cor imager by using a dilution of H3K9me3 nucleosomes (Epicypher, #16-0315), establishing
1003 standard curves for H4 and H3K9me3. Rates were fit to a single exponential rise in GraphPad
1004 Prism software exactly as published[23].

1005

1006 *Phosphatase treatments*

1007 1500 ng of Swi6, pSwi6, and pSwi6$^{S18/24A}$ were incubated for 20 minutes at 37°C with 50 U of
1008 Calf Intestinal Phosphatase (QuickCIP, NEB, M0525S) in 100 mM NaCl, 50 mM Tris-HCl, 10
1009 mM $MgCl_2$, 1 mM dithiothreitol, pH 7.9. Reactions were stopped by boiling in SDS-Laemmli
1010 buffer. For reactions with inactivated CIP, 200U CIP was pre-incubated for 20 minutes at 80°C.
1011 75 ng of Swi6, pSwi6, and pSwi6$^{S18/24A}$ that was either mock-treated, treated with active or
1012 inactivated CIP was separated on either a 15% SDS-PAGE gel or a SuperSep Phos-Tag gel
1013 (Fujifilm, 15.5%, 17 well, 100x100x6.6mm, Lot PAR5302). The Phos-Tag gel was washed with
1014 western transfer buffer with 10 mM EDTA to remove Zn^{2+} ions and then blotted and probed for
1015 Swi6 with Swi6 polyclonal antibody as above.

1016

1017 *Mass Spectrometry*

1018 In-solution Trypsin/Lys C digested peptides were analyzed by online capillary nanoLC-MS/MS
1019 using several different methods. High resolution 1 dimensional LCMS was performed using a 25
1020 cm reversed-phase column fabricated in-house (75 μm inner diameter, packed with ReproSil-
1021 Gold C18-1.9 μm resin (Dr. Maisch GmbH)) that was equipped with a laser-pulled
1022 nanoelectrospray emitter tip. Peptides were eluted at a flow rate of 300 nL/min using a linear
1023 gradient of 2–40% buffer B in 140 min (buffer A: 0.02% HFBA and 5% acetonitrile in water;

1024 buffer B: 0.02% HFBA and 80% acetonitrile in water) in a Thermo Fisher Easy-nLC1200
1025 nanoLC system. Peptides were ionized using a FLEX ion source (Thermo Fisher) using
1026 electrospray ionization into a Fusion Lumos Tribrid Orbitrap Mass Spectrometer (Thermo Fisher
1027 Scientific). Data was acquired in orbi-trap mode. Instrument method parameters were as
1028 follows: MS1 resolution, 120,000 at 200 m/z; scan range, 350−1600 m/z. The top 20 most
1029 abundant ions were subjected to higher-energy collisional dissociation (HCD) or electron
1030 transfer dissociation (ETD) with a normalized collision energy of 35%, activation q 0.25, and
1031 precursor isolation width 2 m/z. Dynamic exclusion was enabled with a repeat count of 1, a
1032 repeat duration of 30 seconds, and an exclusion duration of 20 seconds.
1033 Low-resolution, 1-dimensional LCMS was performed using a nano-LC column packed in a 100-
1034 µm inner diameter glass capillary with an integrated pulled emitter tip. The column consisted of
1035 10 cm of ReproSil-Gold C18-3 µm resin (Dr. Maisch GmbH)). The column was loaded and
1036 conditioned using a pressure bomb. The column was then coupled to an electrospray ionization
1037 source mounted on a Thermo-Fisher LTQ XL linear ion trap mass spectrometer. An Agilent
1038 1200 HPLC equipped with a split line so as to deliver a flow rate of 1 ul/min was used for
1039 chromatography. Peptides were eluted with a 90-minute gradient from 100% buffer A to 60%
1040 buffer B. Buffer A was 5% acetonitrile/0.02% heptafluorobutyric acid (HBFA); buffer B was 80%
1041 acetonitrile/0.02% HBFA. Collision-induced dissociation spectra were collected for each m/z.
1042 Multidimensional protein identification technique (MudPIT) was performed as described[74,75].
1043 Briefly, a 2D nano-LC column was packed in a 100-µm inner diameter glass capillary with an
1044 integrated pulled emitter tip. The column consisted of 10 cm of ReproSil-Gold C18-3 µm resin
1045 (Dr. Maisch GmbH)) and 4 cm strong cation exchange resin (Partisphere, Hi Chrom). The
1046 column was loaded and conditioned using a pressure bomb. The column was then coupled to
1047 an electrospray ionization source mounted on a Thermo-Fisher LTQ XL linear ion trap mass
1048 spectrometer. An Agilent 1200 HPLC equipped with a split line so as to deliver a flow rate of 1
1049 ul/min was used for chromatography. Peptides were eluted using a 4-step gradient with 4
1050 buffers. Buffer (A) 5% acetonitrile, 0.02% heptafluorobutyric acid (HFBA), buffer (B) 80%
1051 acetonitrile, 0.02% HFBA, buffer (C) 250mM NH4AcOH, 0.02% HFBA, (D) 500mM NH4AcOH,
1052 0.02% HFBA. Step 1: 0-80% (B) in 70 min, step 2: 0-50% (C) in 5 min and 0- 45% (B) in 100
1053 min, step 3: 0-100% (C) in 5 min and 0- 45% (B) in 100 min, step 4 0-100% (D) in 5 min and 0-
1054 45% (B) in 160 min. Collision-induced dissociation (CID) spectra were collected for each m/z.
1055 Data analysis: RAW files were analyzed using PEAKS (Bioinformatics Solution Inc) with the
1056 following parameters: semi-specific cleavage specificity at the C-terminal site of R and K,
1057 allowing for 5 missed cleavages, precursor mass tolerance of 15 ppm (3 Da for low-resolution

LCMS), and fragment ion mass tolerance of 0.5 Daltons. Methionine oxidation and phosphorylation of serine, threonine, and tyrosine were set as variable modifications and Cysteine carbamidomethylation was set as a fixed modification. Peptide hits were filtered using a 1% false discovery rate (FDR). Phosphorylation occupancy ratio for amino acids was determined by summing the count of unphosphorylated and phosphorylated amino acids detected in the experiment. We only considered phospho-peptides detected more than once and at least 2% minimal ion intensity.

Estimate of in vivo nucleosome fractions bound

In vitro binding isotherms for nucleosomes (N) can be fit simply via $fraction\ Nbound = \frac{[Swi6]}{[Swi6]+Kd}$. However, this assumes first that [N] << [Swi6] and << K_d, such that [Swi6] total ≈ [Swi6] free. In the nucleus, these assumptions do not hold. However, a quadratic equation[48] can be used to estimate N bound, accounting for bound Swi6. In this case,

$$frNbound = \frac{[N]total+[Swi6]total+Kd-\sqrt{([N]total+[Swi6]total+Kd)^2-4*[N]total*[Swi6]total}}{2*[N]total}$$

. To estimate the fraction of unmethylated nucleosomes bound by pSwi6 or unpSwi6, we used K_ds from Figure 4F, total Swi6 concentrations of 2.1-4.6μM, and total nucleosome contraction estimate of ~10μM.

Data availability statement:

ChIP-Seq data is deposited at NIH GEO Record GSE271394. The following secure token has been created to allow review, while it remains in private status: kvwbksygjhebfyj

Figure 1

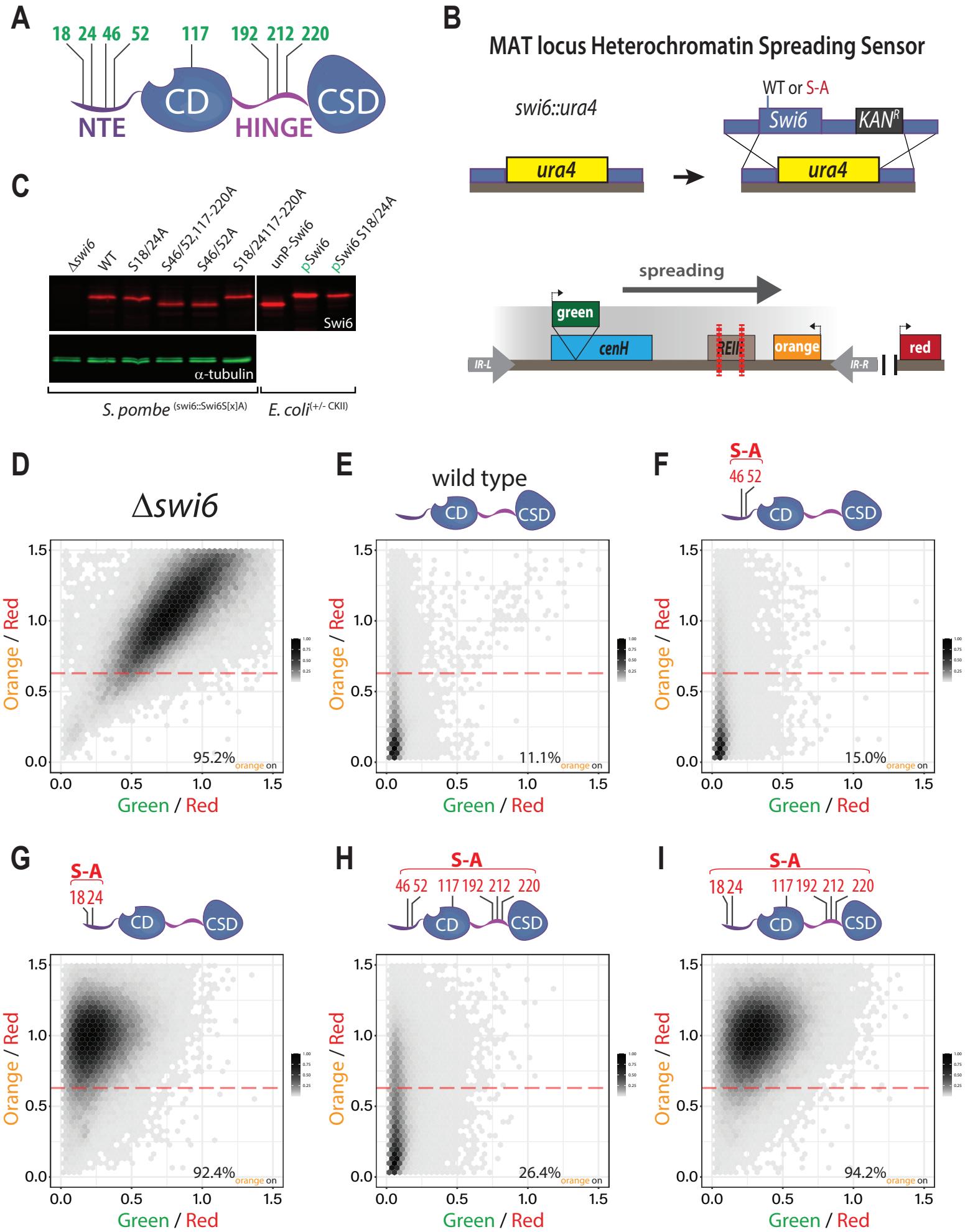
A
18 24 46 52
117
192 212 220
NTE
CD
HINGE
CSD
B
MAT locus Heterochromatin Spreading Sensor
swi6::ura4
ura4
WT or S-A
Swi6
KAN^R
ura4
spreading
green
cenH
REII
orange
red
IR-L
IR-R
C
Δswi6
WT
S18/24A
S46/52,117-220A
S46/52A
S18/24117-220A
unP-Swi6
pSwi6
pSwi6 S18/24A
Swi6
α-tubulin
S. pombe (swi6::Swi6S[x]A)
E. coli (+/- CKII)
D
Δswi6
95.2%
orange on
E
wild type
11.1%
orange on
F
S-A
46 52
15.0%
orange on
G
S-A
18 24
92.4%
orange on
H
S-A
46 52 117 192 212 220
26.4%
orange on
I
S-A
18 24 117 192 212 220
94.2%
orange on
Orange / Red
Green / Red
0.0
0.5
1.0
1.5

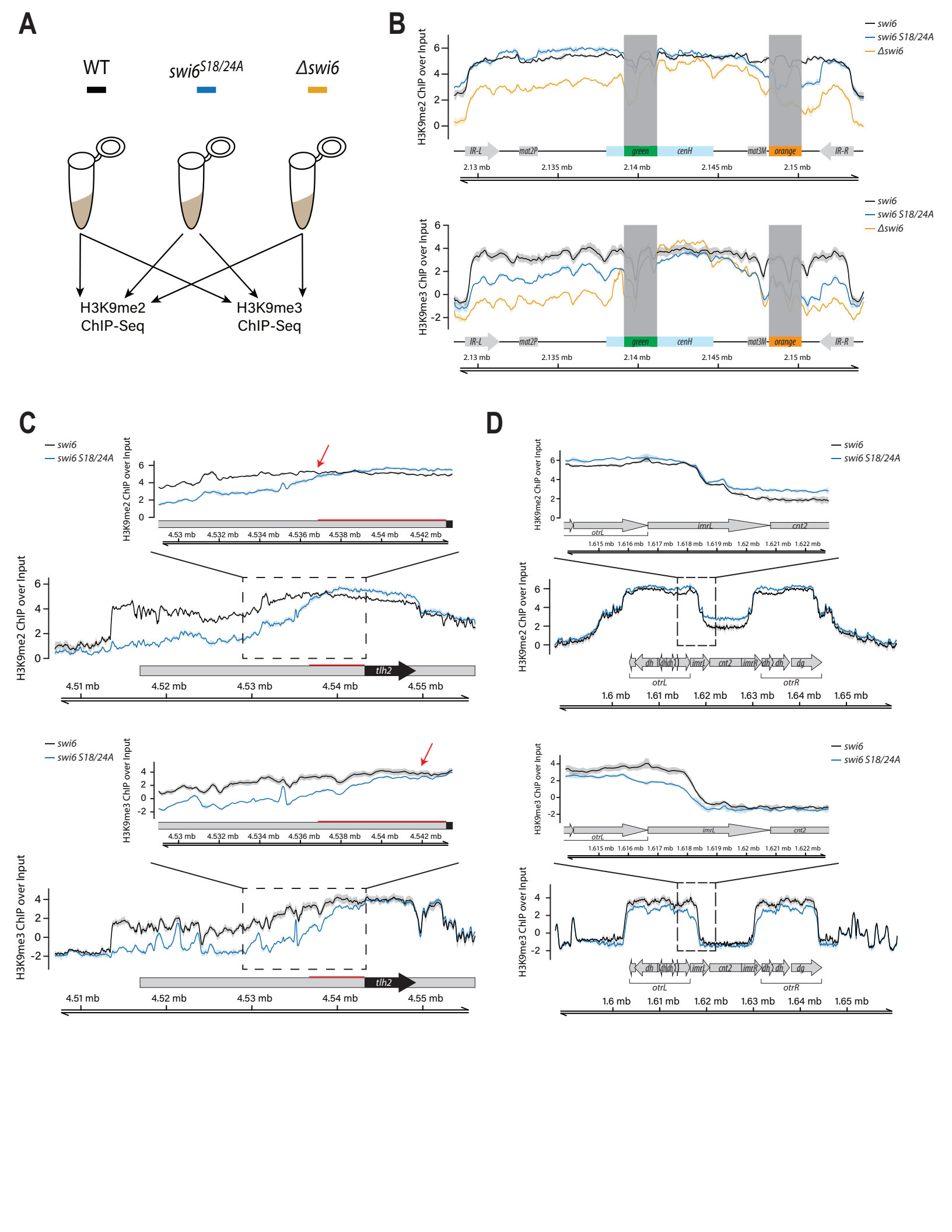
A
WT
swi6S18/24A
Δswi6
H3K9me2 ChIP-Seq
H3K9me3 ChIP-Seq
B
swi6
swi6 S18/24A
Δswi6
H3K9me2 ChIP over Input
H3K9me3 ChIP over Input
IR-L
mat2P
green
cenH
mat3M
orange
IR-R
2.13 mb
2.135 mb
2.14 mb
2.145 mb
2.15 mb
C
swi6
swi6 S18/24A
H3K9me2 ChIP over Input
H3K9me3 ChIP over Input
tlh2
4.51 mb
4.52 mb
4.53 mb
4.54 mb
4.55 mb
D
otrL
imrL
cnt2
dh
dhdh
imrR
dg
otrR
1.6 mb
1.61 mb
1.62 mb
1.63 mb
1.64 mb
1.65 mb

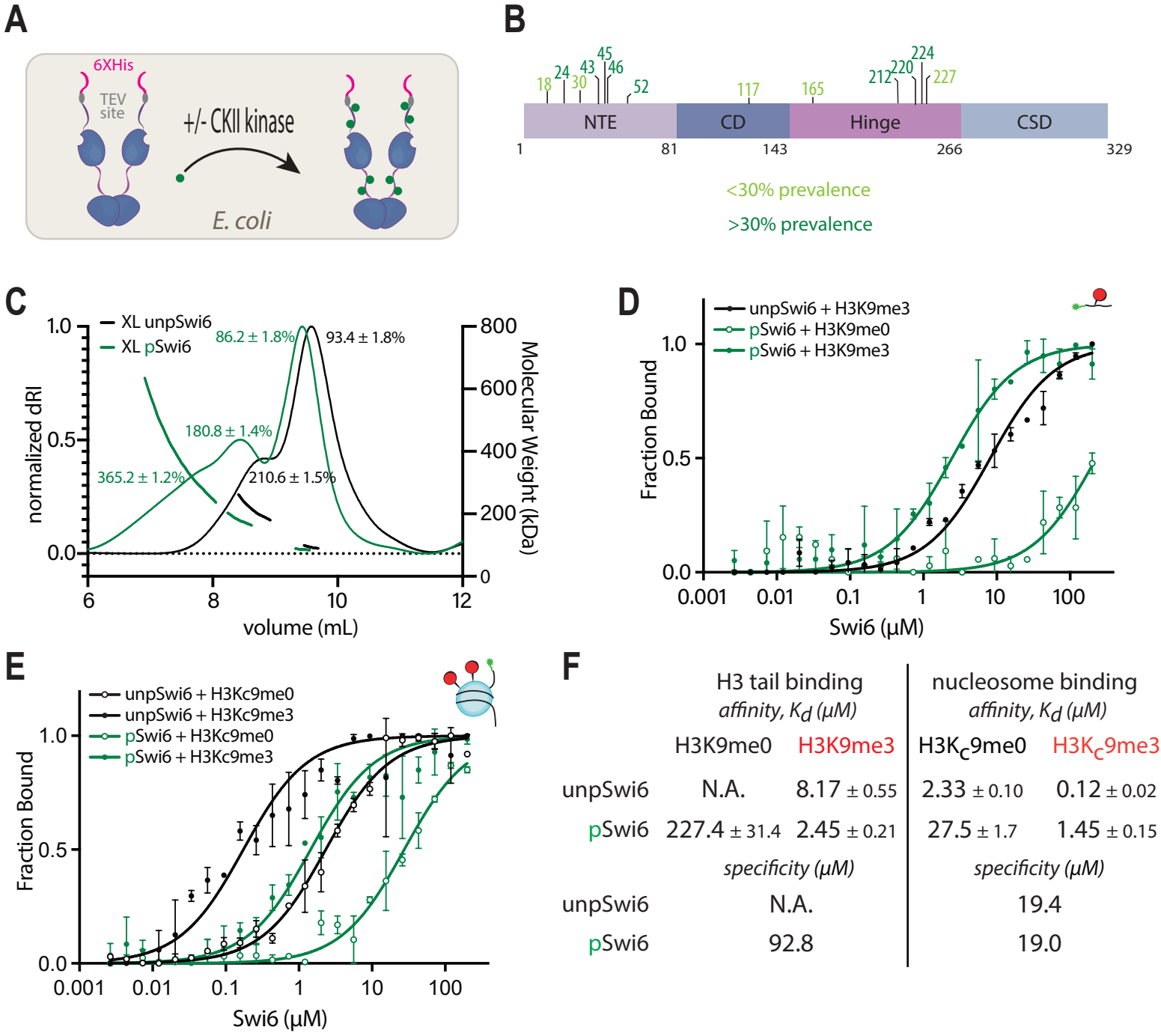

	H3 tail binding affinity, K_d (μM)		nucleosome binding affinity, K_d (μM)	
	H3K9me0	H3K9me3	$H3K_c9me0$	$H3K_c9me3$
unpSwi6	N.A.	8.17 ± 0.55	2.33 ± 0.10	0.12 ± 0.02
pSwi6	227.4 ± 31.4	2.45 ± 0.21	27.5 ± 1.7	1.45 ± 0.15
	specificity (μM)		*specificity (μM)*	
unpSwi6	N.A.		19.4	
pSwi6	92.8		19.0	

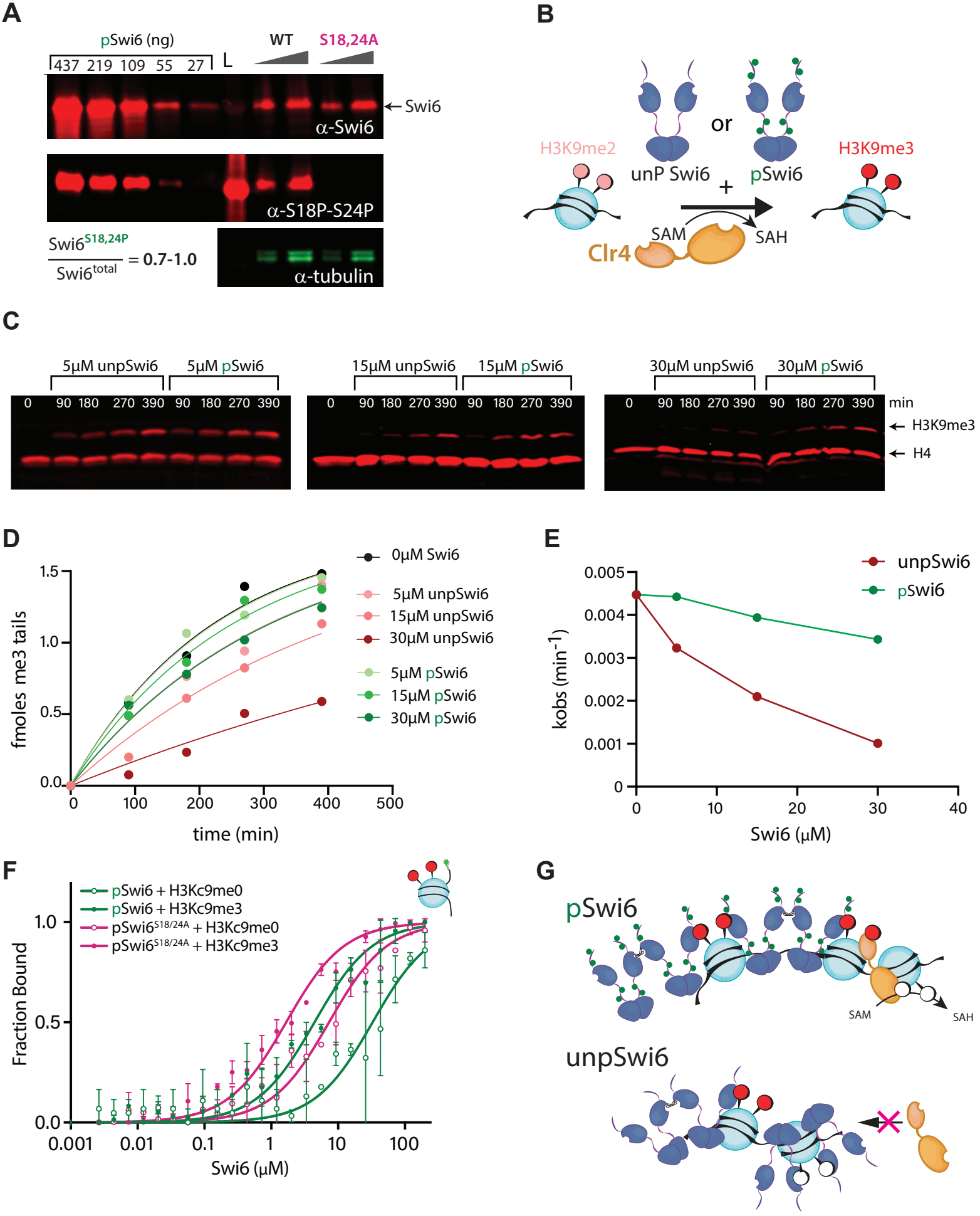
A
pSwi6 (ng)
437 219 109 55 27
L
WT
S18,24A
Swi6
α-Swi6
α-S18P-S24P
Swi6S18,24P / Swi6total = 0.7-1.0
α-tubulin
B
H3K9me2
unP Swi6
or
pSwi6
H3K9me3
+
SAM
SAH
Clr4
C
5μM unpSwi6
5μM pSwi6
15μM unpSwi6
15μM pSwi6
30μM unpSwi6
30μM pSwi6
0 90 180 270 390 90 180 270 390
min
H3K9me3
H4
D
fmoles me3 tails
time (min)
0μM Swi6
5μM unpSwi6
15μM unpSwi6
30μM unpSwi6
5μM pSwi6
15μM pSwi6
30μM pSwi6
E
kobs (min-1)
Swi6 (μM)
unpSwi6
pSwi6
F
Fraction Bound
Swi6 (μM)
pSwi6 + H3Kc9me0
pSwi6 + H3Kc9me3
pSwi6S18/24A + H3Kc9me0
pSwi6S18/24A + H3Kc9me3
G
pSwi6
SAM
SAH
unpSwi6

SFigure 1

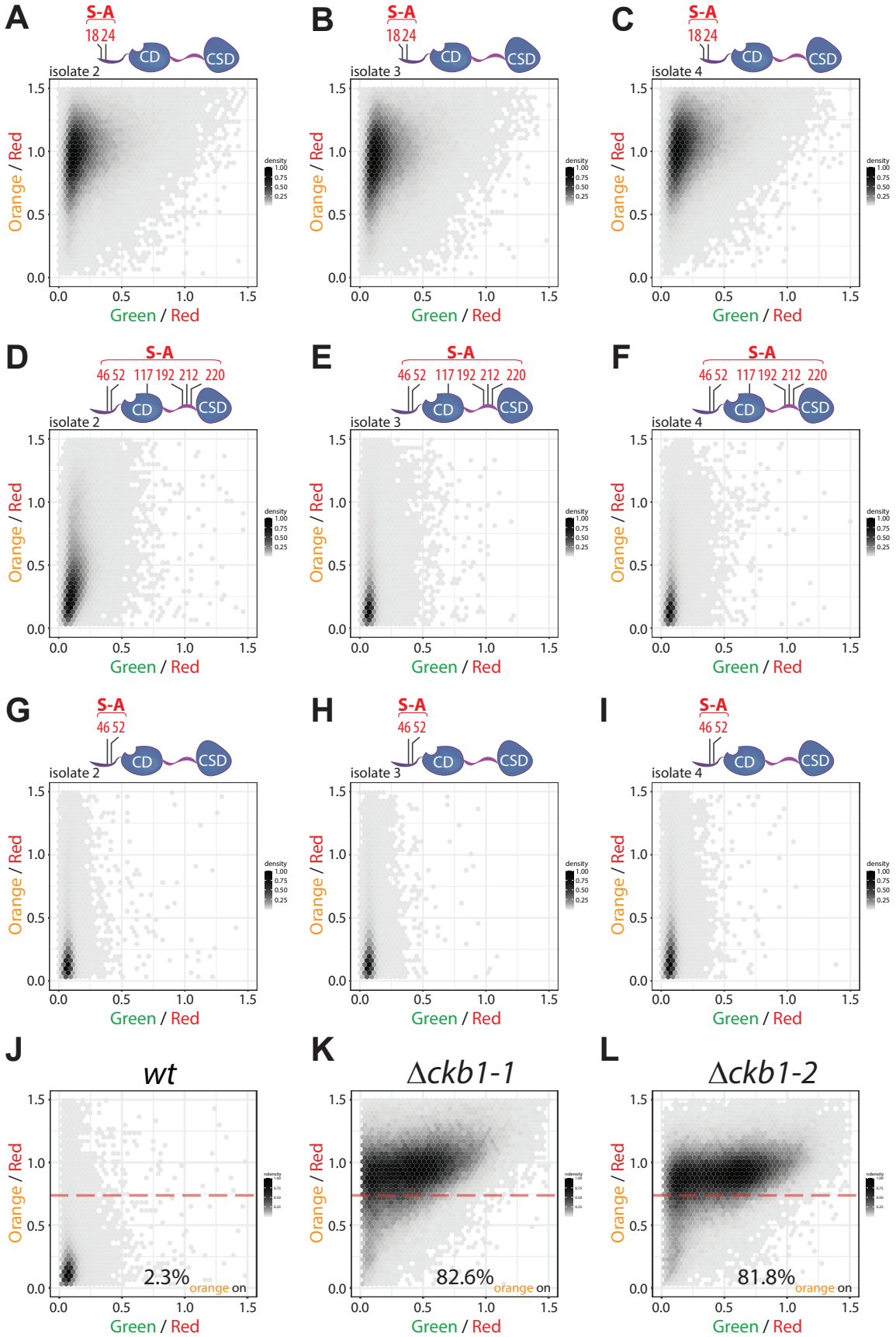
A
S-A
18 24
CD
CSD
isolate 2
B
isolate 3
C
isolate 4
D
46 52 117 192 212 220
E
F
G
46 52
H
I
J
wt
K
Δckb1-1
L
Δckb1-2
Orange / Red
Green / Red
density
2.3%
82.6%
81.8%
orange on

SFigure 2

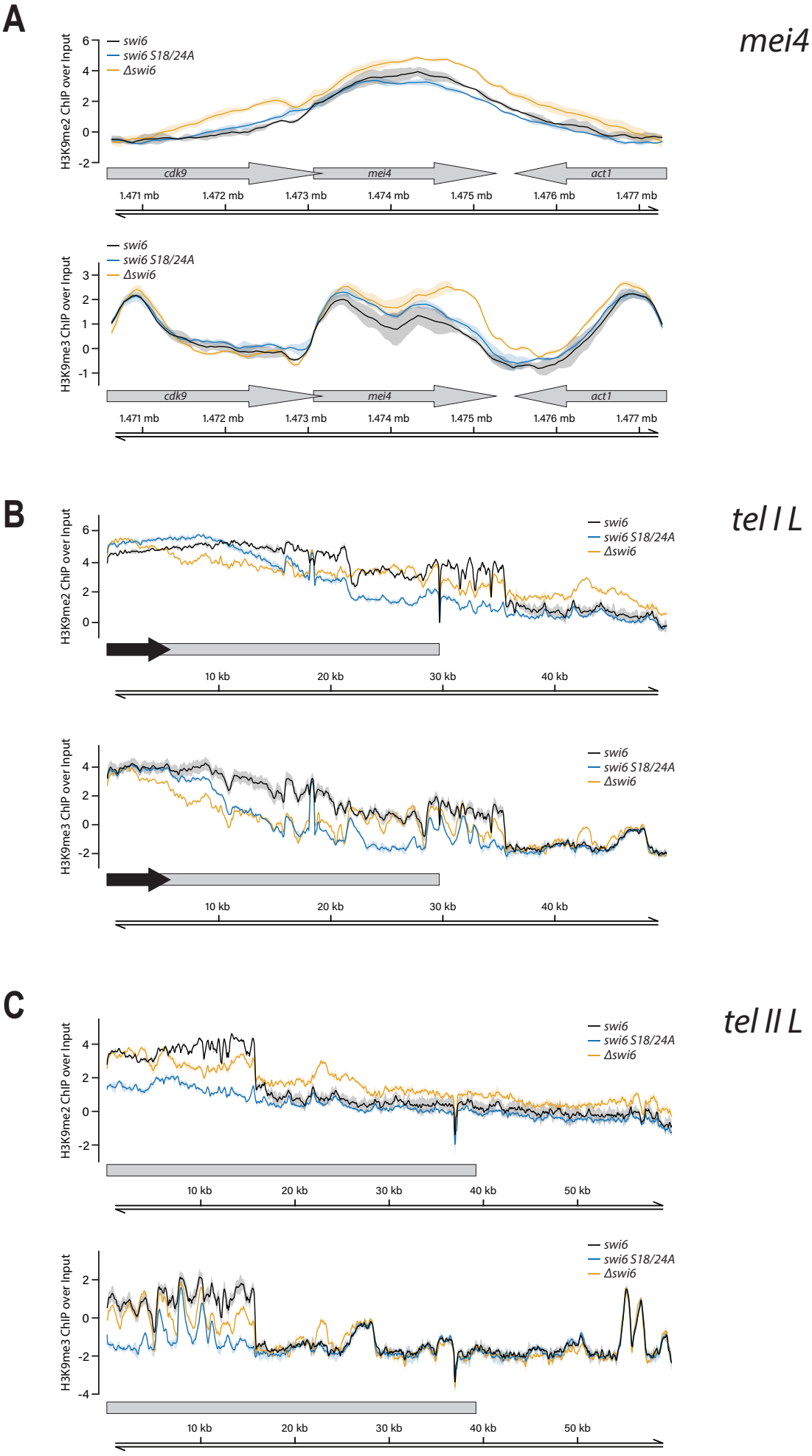
A
mei4
H3K9me2 ChIP over Input
swi6
swi6 S18/24A
Δswi6
cdk9
mei4
act1
1.471 mb
1.472 mb
1.473 mb
1.474 mb
1.475 mb
1.476 mb
1.477 mb
H3K9me3 ChIP over Input
B
tel I L
10 kb
20 kb
30 kb
40 kb
C
tel II L
50 kb

SFigure 3

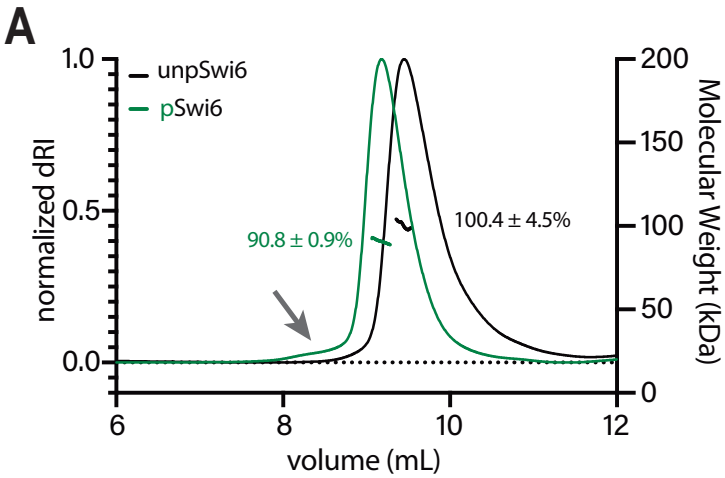

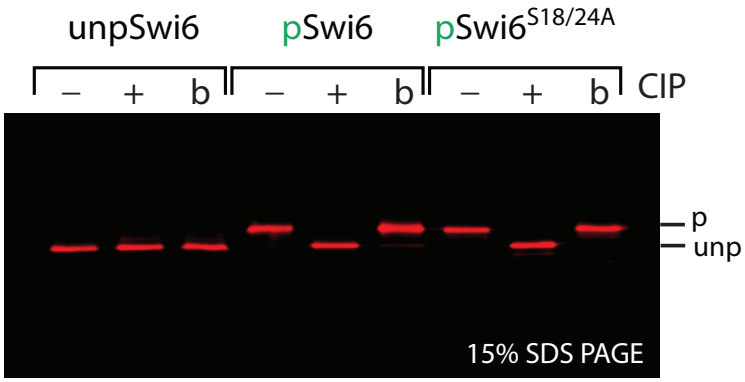

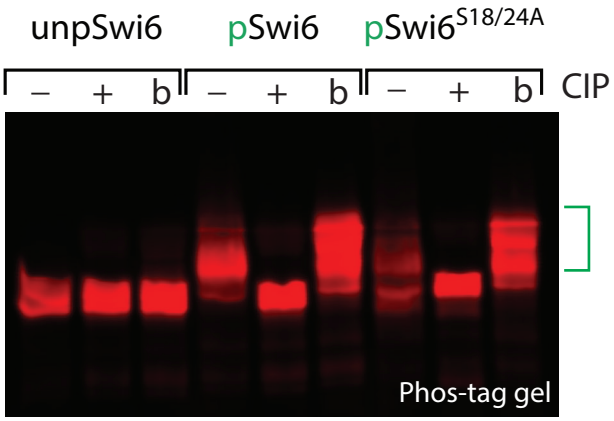

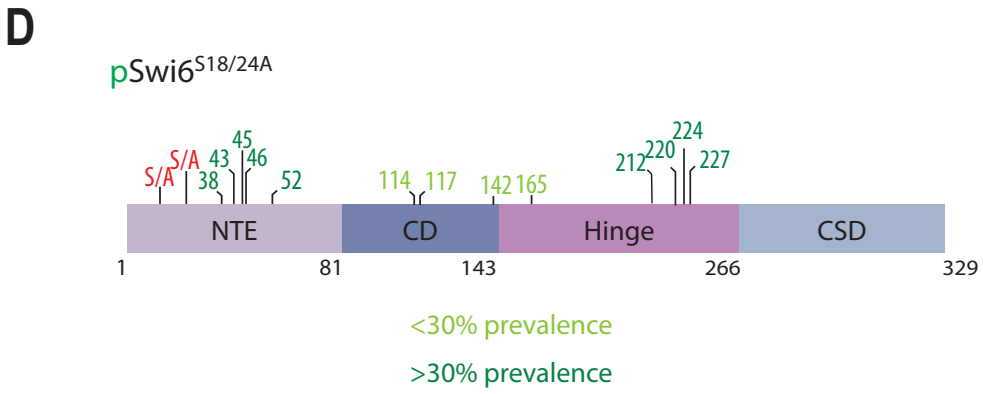

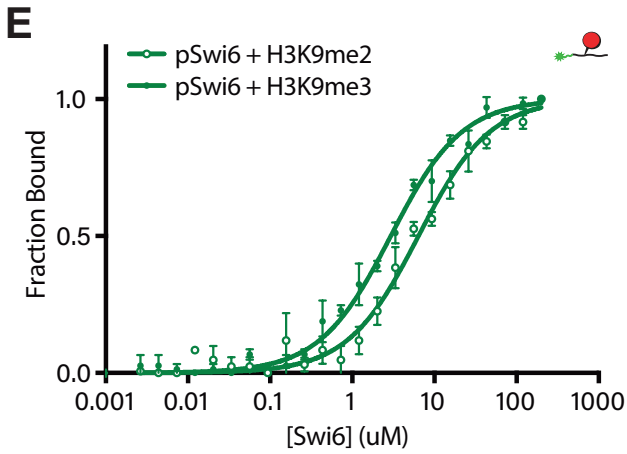

H3 tail binding
affinity, K_d (μM)

H3K9me2	H3K9me3
6.40 ± 0.41	2.94 ± 0.14

SFigure 4

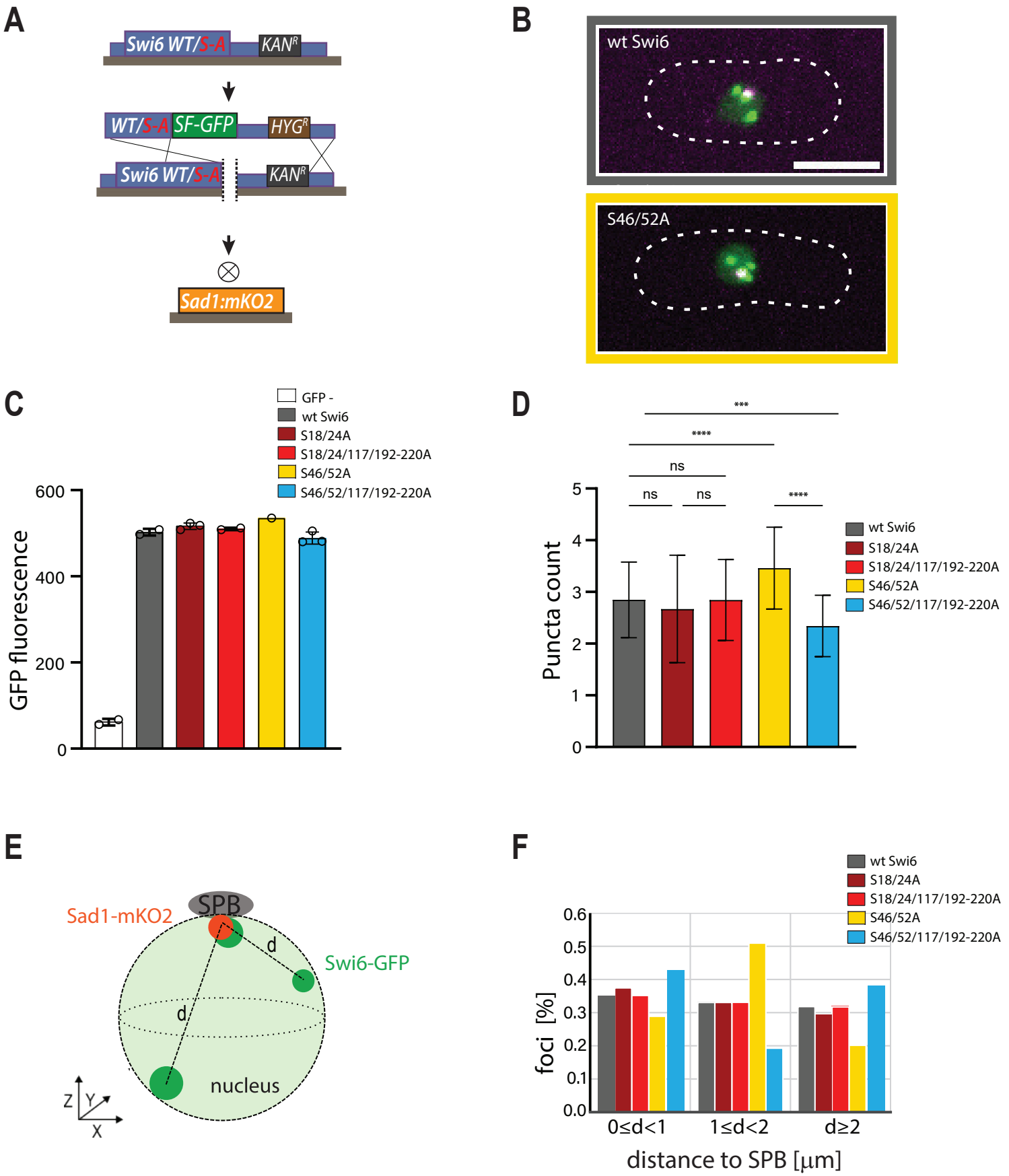
A
Swi6 WT/S-A
KAN^R
WT/S-A
SF-GFP
HYG^R
Swi6 WT/S-A
KAN^R
Sad1:mKO2
B
wt Swi6
S46/52A
C
GFP -
wt Swi6
S18/24A
S18/24/117/192-220A
S46/52A
S46/52/117/192-220A
GFP fluorescence
600
400
200
0
D
***
****
ns
ns
ns
****
Puncta count
5
4
3
2
1
0
wt Swi6
S18/24A
S18/24/117/192-220A
S46/52A
S46/52/117/192-220A
E
SPB
Sad1-mKO2
d
Swi6-GFP
d
nucleus
Z
Y
X
F
wt Swi6
S18/24A
S18/24/117/192-220A
S46/52A
S46/52/117/192-220A
foci [%]
0.6
0.5
0.4
0.3
0.2
0.1
0.0
0≤d<1
1≤d<2
d≥2
distance to SPB [µm]

SFigure 5

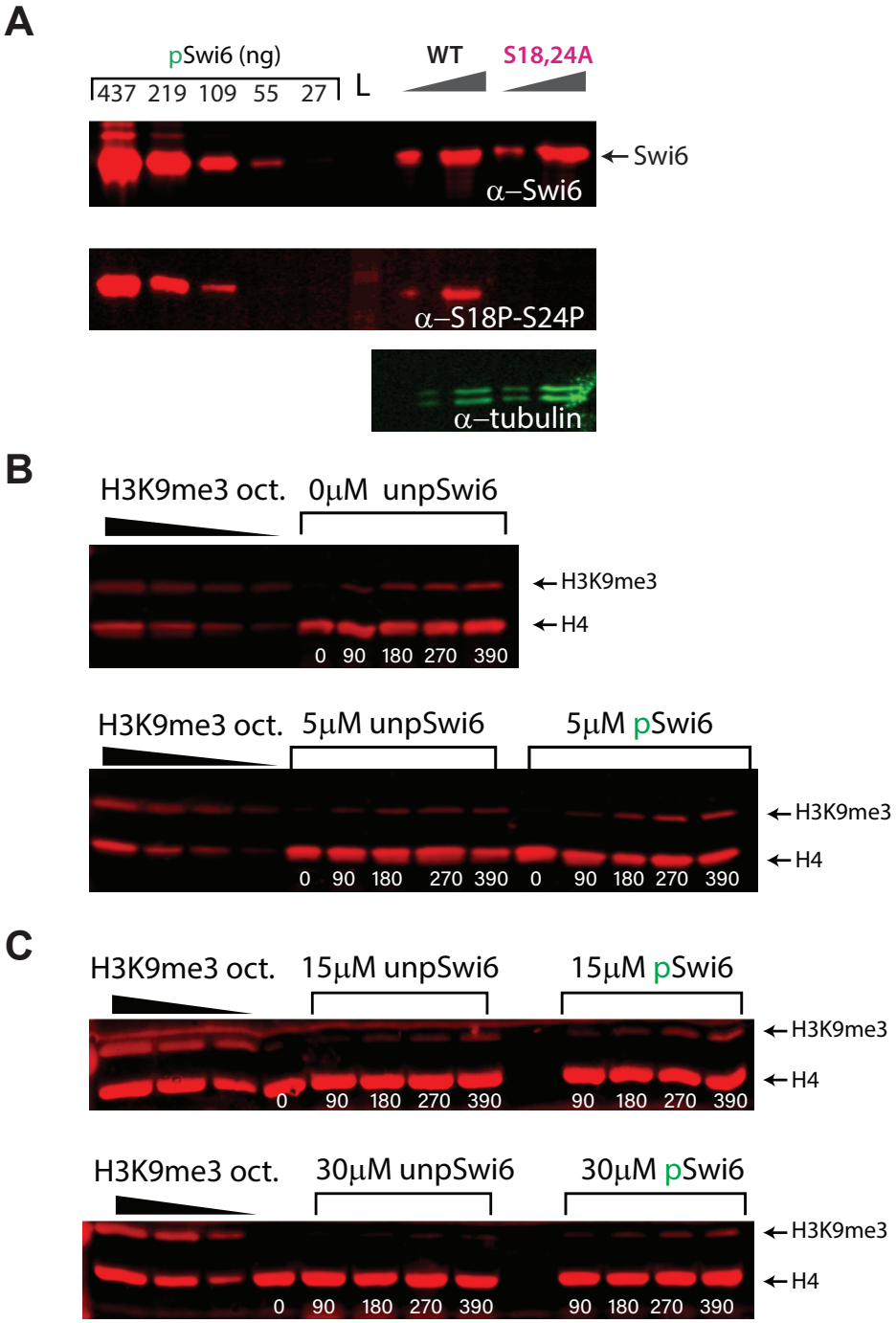
A
pSwi6 (ng)
437 219 109 55 27
L
WT
S18,24A
Swi6
α–Swi6
α–S18P-S24P
α–tubulin
B
H3K9me3 oct.
0μM unpSwi6
H3K9me3
H4
0 90 180 270 390
H3K9me3 oct.
5μM unpSwi6
5μM pSwi6
H3K9me3
H4
0 90 180 270 390 0 90 180 270 390
C
H3K9me3 oct.
15μM unpSwi6
15μM pSwi6
H3K9me3
H4
0 90 180 270 390 90 180 270 390
H3K9me3 oct.
30μM unpSwi6
30μM pSwi6
H3K9me3
H4
0 90 180 270 390 90 180 270 390

Supporting Table 1

	Mononucleosome binding	
	relative affinity	
	H3K$_c$9me0	H3K$_c$9me3
pSwi6	7.48 ± 1.07	**1 ± 0.1**
pSwi6$^{S18/24A}$	1.67 ± 0.15	0.38 ± 0.003
	specificity	
pSwi6	7.48	
pSwi6$^{S18/24A}$	4.39	

Supporting Table 2

Yeast strains used in this study

Identifier	Genotype	Figure; experiment	Source
PAS210	h+, *sad1*:mKO2:NATMX	Fig. 3G, H; SFig.4	Al-Sady et al 2016
PAS332	h90, cenH:: ade6p:SF-GFP (Kint2); mat3m(EcoRV):: ade6p:mKO2; ade6p:3xE2C:hygMX at Locus2; ΔREIII::REIII(Δs1, Δs2)	Fig. S1J	Greenstein et al 2018
PAS807	h90, cenH:: ade6p:SF-GFP (Kint2); mat3m(EcoRV):: ade6p:mKO2; ade6p:3xE2C:hygMX at Locus2; ΔREIII::REIII(Δs1, Δs2), *swi6::ura4*	Fig. 1C,D; Fig. 2B; SFig. A-C	This study
PAS814	h90, cenH:: ade6p:SF-GFP (Kint2); mat3m(EcoRV):: ade6p:mKO2; ade6p:3xE2C:hygMX at Locus2; ΔREIII::REIII(Δs1, Δs2), *swi6*:KANMX	Fig. 1C,E; Fig. 2B-D; SFig. A-C	This study
PAS851,858, 859, 860 (isolates)	h90, cenH:: ade6p:SF-GFP (Kint2); mat3m(EcoRV):: ade6p:mKO2; ade6p:3xE2C:hygMX at Locus2; ΔREIII::REIII(Δs1, Δs2), *swi6S18/24A*:KANMX	Fig. 1C,G; SFig.1A-C; Fig. 2B-D; SFig. A-C	This study
PAS852, 861,862, 863 isolates)	h90, cenH:: ade6p:SF-GFP (Kint2); mat3m(EcoRV):: ade6p:mKO2; ade6p:3xE2C:hygMX at Locus2; ΔREIII::REIII(Δs1, Δs2), *swi6S46/52,117-220A*:KANMX	Fig. 1C,H; SFig.1D-F	This study
PAS853, 864, 865, 866 (isolates)	h90, cenH:: ade6p:SF-GFP (Kint2); mat3m(EcoRV):: ade6p:mKO2; ade6p:3xE2C:hygMX at Locus2; ΔREIII::REIII(Δs1, Δs2), *swi6S46/52*:KANMX	Fig. 1C,F	This study
PAS854	h90, cenH:: ade6p:SF-GFP (Kint2); mat3m(EcoRV):: ade6p:mKO2; ade6p:3xE2C:hygMX at Locus2; ΔREIII::REIII(Δs1, Δs2), *swi6S18/24,117-220A*:KANMX	Fig. 1C,I	This study
PAS909	*sad1*:mKO2:NATMX; *swi6S46/52*:SF-GFP:HYGMX	SFig4B-F	This study
PAS910,911	*sad1*:mKO2:NATMX; *swi6S18/24,117-220A*:SF-GFP:HYGMX	Fig3G,H; SFig4C-F	This study
PAS913	*sad1*:mKO2:NATMX; *swi6*:SF-GFP:HYGMX	Fig3G,H; SFig4C-F	This study
PAS919	*sad1*:mKO2:NATMX; *swi6S18/24*:SF-GFP:HYGMX	Fig3G,H; SFig4C-F	This study
PAS922	*sad1*:mKO2:NATMX; *swi6S46/52,117-220A*:SF-GFP:HYGMX	Fig3G,H; SFig4C-F	This study
PAS1189	h90, cenH:: ade6p:SF-GFP (Kint2); mat3m(EcoRV):: ade6p:mKO2; ade6p:3xE2C:hygMX at Locus2; ΔREIII::REIII(Δs1, Δs2), *ckb1::*KANMX	Fig. S1K,L	This study